SPECIAL
PECAN
COLLECTION

Origins of Vorticity in a Simulated Tornadic Mesovortex Observed during PECAN on 6 July 2015

MATTHEW D. FLOURNOY

School of Meteorology, University of Oklahoma, Norman, Oklahoma

MICHAEL C. CONIGLIO

NOAA/National Severe Storms Laboratory, and School of Meteorology, University of Oklahoma, Norman, Oklahoma

(Manuscript received 27 June 2018, in final form 12 October 2018)

ABSTRACT

To better understand and forecast nocturnal thunderstorms and their hazards, an expansive network of fixed and mobile observing systems was deployed in the summer of 2015 for the Plains Elevated Convection at Night (PECAN) field experiment to observe low-level jets, convection initiation, bores, and mesoscale convective systems. On 5–6 July 2015, mobile radars and ground-based surface and upper-air profiling systems sampled a nocturnal, quasi-linear convective system (QLCS) over South Dakota. The QLCS produced several severe wind reports and an EF-0 tornado. The QLCS and its environment leading up to the mesovortex that produced this tornado were well observed by the PECAN observing network. In this study, observations from radiosondes, Doppler radars, and aircraft are assimilated into an ensemble analysis and forecasting system to analyze this event with a focus on the development of the observed tornadic mesovortex. All ensemble members simulated low-level mesovortices with one member in particular generating two mesovortices in a manner very similar to that observed. Forecasts from this member were analyzed to examine the processes increasing vertical vorticity during the development of the tornadic mesovortex. Cyclonic vertical vorticity was traced to three separate airstreams: the first from southerly inflow that was characterized by tilting of predominantly crosswise horizontal vorticity along the gust front, the second from the north that imported streamwise horizontal vorticity directly into the low-level updraft, and the third from a localized downdraft/rear-inflow jet in which the horizontal vorticity became streamwise during descent. The cyclonic vertical vorticity then intensified rapidly through intense stretching as the parcels entered the low-level updraft of the developing mesovortex.

1. Introduction

Mechanisms responsible for the development of significant low-level[1] rotation and mesovortices in quasi-linear convective systems (QLCSs) have been studied for decades. Mesovortices are typically meso-γ-scale (Orlanski 1975; 2–20 km) phenomena, extend up to 3 km above ground level (AGL), and persist for no more than an hour. These features distinguish mesovortices from other convectively induced, midtropospheric vortices, including bookend vortices (e.g., Weisman 1993) and mesoscale convective vortices (MCVs; e.g., Menard and Fritsch 1989; Cotton et al. 1989), which are typically 20–200 km in length and can persist for several hours. Mesovortices are typically most intense near the surface (1–2 km AGL), thus explaining their association with straight-line surface wind damage and, occasionally, tornadoes. This inherent severe weather threat associated with mesovortices has made them the subject of many studies, which have yielded multiple theories as to how they form and produce strong winds and tornadoes.

a. Mesovortices in QLCSs

Numerous observational studies have shown that mesovortices are associated with severe surface winds

[1] In this paper, the term "low level" is used to describe features in the 500–2000-m AGL layer.

Corresponding author: Matthew Flournoy, matthew.flournoy@noaa.gov

DOI: 10.1175/MWR-D-18-0221.1

within QLCSs (e.g., Forbes and Wakimoto 1983; Funk et al. 1999; Przybylinski et al. 2000; Atkins et al. 2004, 2005; Wakimoto et al. 2006b; Schenkman et al. 2011a; Mahale et al. 2012; Newman and Heinselman 2012). Such mesovortex-induced wind events tend to be localized in space and time, on the order of tens of kilometers and minutes, and can develop very quickly within QLCSs (Mahale et al. 2012; Newman and Heinselman 2012). Because of this, forecasting severe wind associated with mesovortices is a difficult problem, and the study of both (i) synoptic conditions conducive for the development of mesovortices and (ii) mechanisms forcing mesovortex genesis in QLCSs remain active areas of research.

Given favorable thermodynamic conditions, 15–20 m s^{-1} of line-normal vertical wind shear in the lowest 5 km of the environment is conducive for the development of mesovortices (Weisman and Trapp 2003). These values are qualitatively consistent with Rotunno–Klemp–Weisman (RKW) theory (Rotunno et al. 1988), which explains how strong cold pool–forced updrafts result from a balance between cold pool and low-level environmental vertical wind shear oriented normal to the convective line. Whereas a stronger cold pool–forced updraft plays a role in the structure and intensity of the convective line, a stronger forced updraft could also favor mesovortices through increased vertical vorticity stretching and intensification. Quasi-idealized simulations of observed mesovortices have yielded similar results, with stronger mesovortices forming when low-level environmental wind shear appeared to sufficiently balance cold pool shear (Atkins and St. Laurent 2009a). These results agree with the observational study of Schaumann and Przybylinski (2012), who found that intense mesovortices capable of producing tornadoes are more likely when wind shear is oriented normal to the convective line in the lowest 3 km. In other modeling studies, Snook et al. (2011) and Schenkman et al. (2011b) found that an accurate representation of low-level environmental shear was crucial for capturing the location and intensity of mesovortices. Although mesovortex generation is strongly associated with low-level shear, mesoscale heterogeneities (Wheatley and Trapp 2008) and storm-generated features (Newman and Heinselman 2012) can also play a role.

One of the first studies investigating QLCS mesovortex formation on the mesoscale hypothesized that shear instability played a primary role (Forbes and Wakimoto 1983). Some later studies came to the same conclusion (Przybylinski 1995; Wheatley and Trapp 2008), showing that the release of horizontal shear instability (Miles and Howard 1964) along a system-generated gust front served as the precursor to mesovortex development. The vertical vorticity relied upon for the shear instability mechanism originated from upward tilting of environmental horizontal vorticity (Wheatley and Trapp 2008). This has also been shown theoretically by Lee and Wilhelmson (1997a,b), who found misovortices (and tornado-like vortices) to form along a dry outflow boundary via vortex sheet rollup, subharmonic interactions, and consolidation of dominant vortices. Although this mechanism may be important for the genesis of some QLCS mesovortices, many have been observed to form in isolation, in cyclonic–anticyclonic couplets, or at spacings along the gust front not predicted by a horizontal shear instability mechanism, suggesting that other processes must be at least partially responsible (e.g., Trapp and Weisman 2003; Atkins and St. Laurent 2009b; Schenkman et al. 2012; Xu et al. 2015).

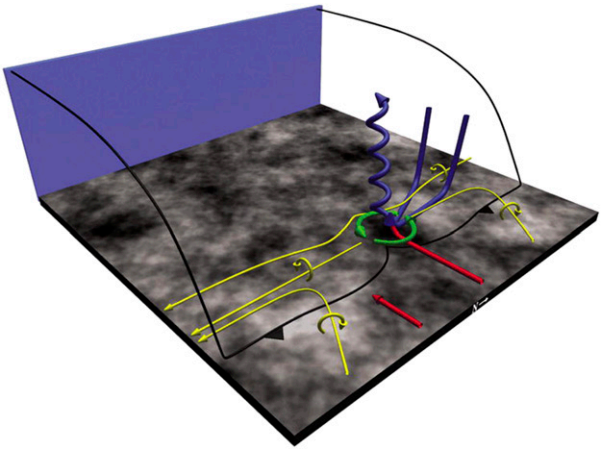

FIG. 1. Schematic showing the formation of a cyclonic MV via the "supercell mechanism" by Atkins and St. Laurent (2009b; e.g., tilting and stretching of low-level horizontal and vertical vorticity transported to the surface by a downdraft). Blue and red arrows represent storm-internal and environmental airflow, respectively, and gold arrows represent low-level horizontal vortex lines. The green arrows show the location of the cyclonic MV.

One of these mechanisms for mesovortex formation in QLCSs is the tilting of baroclinic vorticity generated internally along the cold pool interface by an updraft or downdraft. This process generates a couplet of positive and negative vertical vorticity along the gust front, with the orientation of the couplet dependent upon whether an updraft (Atkins and St. Laurent 2009b) or downdraft (Bernardet and Cotton 1998; Trapp and Weisman 2003; Wheatley and Trapp 2008; Richter et al. 2014) serves as the tilting agent.

A third mechanism for mesovortex formation in QLCSs (specifically for isolated, cyclonic mesovortices) is the tilting and stretching of low-level, predominantly streamwise horizontal vorticity by an updraft. This process differs from that responsible for the formation of mesovortex couplets because the updraft becomes

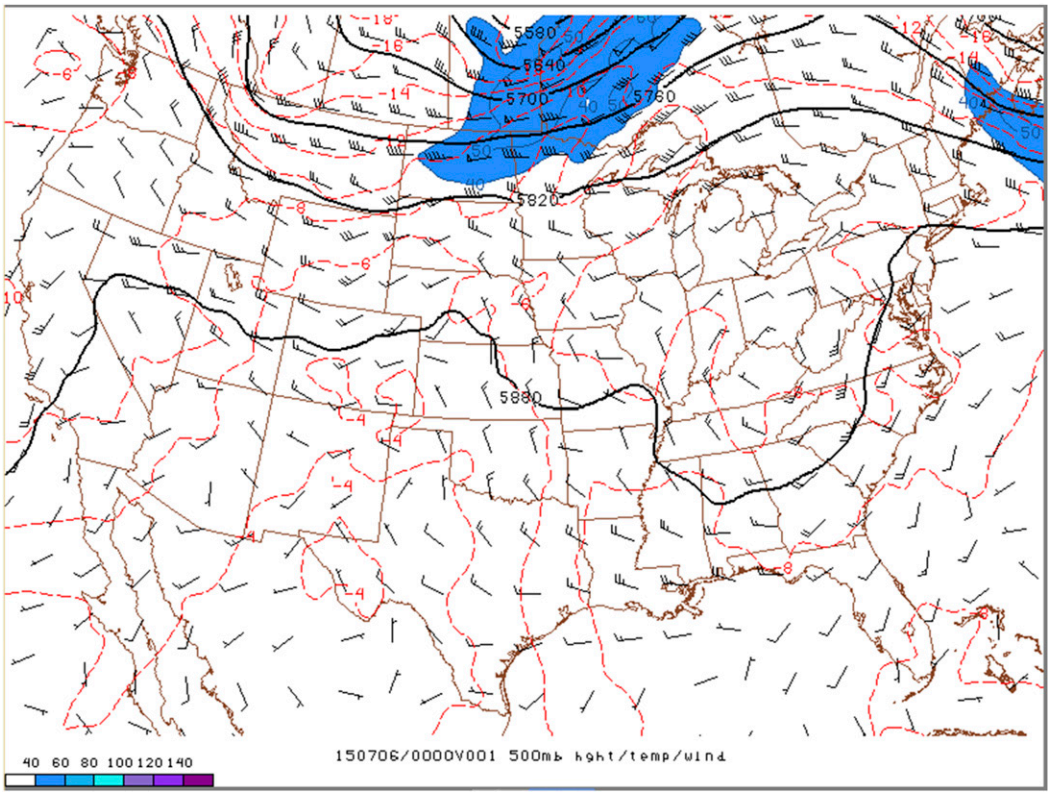

FIG. 2. The 500-hPa geopotential heights (black lines every 60 m), temperature (dashed red lines every 2°C), and winds (full barb = 10 kt) from the RAP analysis valid at 0000 UTC 6 Jul 2015 (from the Storm Prediction Center archive).

collocated with the vertical vorticity maximum, producing a single rotating updraft (Fig. 1). This low-level vertical vorticity is typically generated by tilting of horizontal vorticity in association with a downdraft (e.g., Atkins and St. Laurent 2009b; Parker and Dahl 2015) along an internal boundary (i.e., the system gust front) or an external boundary with preexisting vertical vorticity (Przybylinski et al. 2000; Schenkman et al. 2011b) prior to encountering the low-level updraft. These mechanisms and the resulting collocation of the updraft and cyclonic vorticity resemble the processes responsible for the formation of low- and midlevel mesocyclones and tornadoes in supercells (e.g., Markowski and Richardson 2009).

Recent studies add that horizontal vorticity generated by surface friction may be an important source for mesovortex generation. In real-data simulations of a nocturnal QLCS, Schenkman et al. (2012) concluded that both surface friction and boundary layer stability played a role in the development of an intense, low-level ''rotor'' of horizontal vorticity just behind the gust front. The upward branch of this rotor coincided with an intense mesovortex and tornado-like vortex. In a similar study, Xu et al. (2015) found a large residual horizontal vorticity tendency after accounting for the effects of tilting, stretching, and baroclinicity along parcel trajectories; the study presumed that the residual vorticity tendency was largely the result of frictional effects, as opposed to errors in the other budget terms. The authors concluded that frictionally generated vorticity contributed significantly to the development of a mesovortex in a QLCS. Frictional effects have also recently been shown to serve as an important source of vorticity in supercellular mesocyclones and tornadoes in modeling studies (Schenkman et al. 2014; Markowski 2016; Mashiko 2016b; Roberts et al. 2016); however, Markowski and Bryan (2016) found that the use of large-eddy simulations may result in the development of unrealistically large near-surface shear in unstratified, horizontally homogeneous, quasi-steady boundary layers if the flow is not sufficiently turbulent. Thus, the role of surface friction as an important vorticity source in convective environments remains a relatively unexplored, active area of research.

Many of the above processes responsible for the generation of mesovortices can be augmented by the

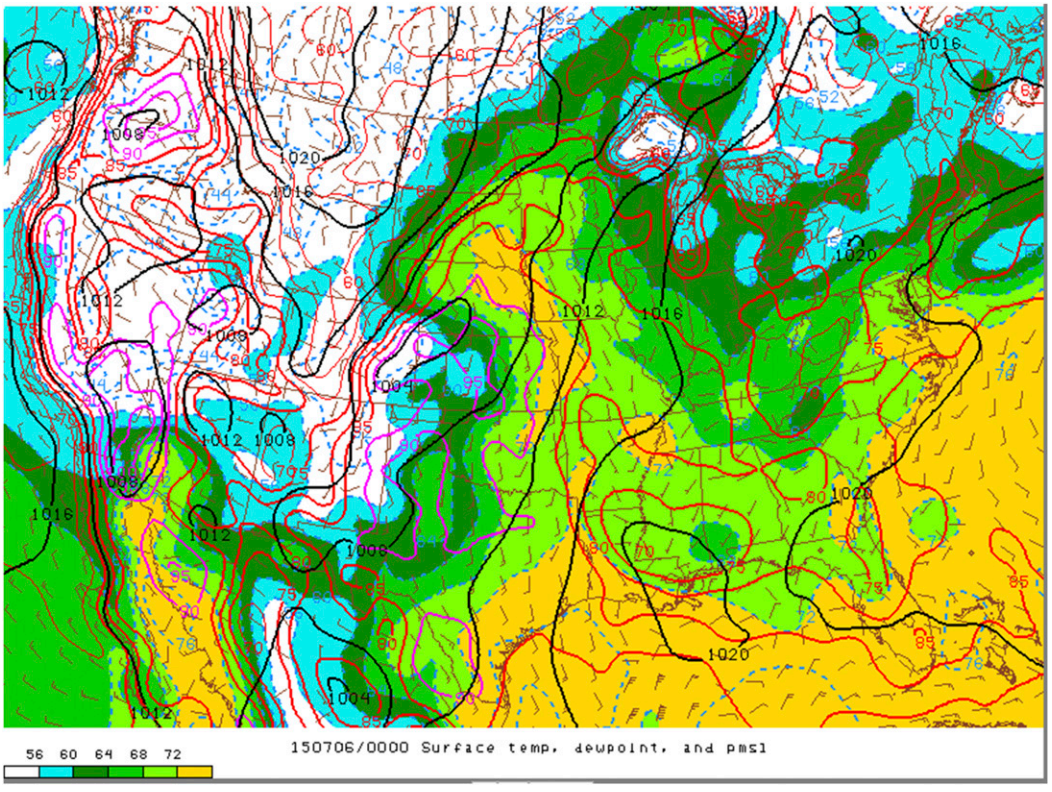

FIG. 3. As in Fig. 2, but for 2-m temperature (red and magenta contours every 5°F), 2-m dewpoint temperature (blue dashed contours shaded every 4°F), and pressure reduced to mean sea level (black contours every 4 hPa).

presence of a rear-inflow jet (RIJ), a relatively common feature of mature QLCSs (Weisman 1992) that is frequently associated with severe winds at the surface. Severe winds may or may not be associated with low-level mesovortices, but when they are, the strongest winds are typically found within the equatorward portion of the mesovortex (Atkins and St. Laurent 2009a), where the motion of the system, enhanced winds in the RIJ, and internal circulation of the cyclonic mesovortex are all oriented in the same direction (Wakimoto et al. 2006a). RIJs often descend toward the leading edge of the QLCS, which can enhance convergence at the gust front and subsequent low-level updrafts, vorticity tilting, and stretching, and result in more intense mesovortices (Atkins et al. 2005; Schaumann and Przybylinski 2012; Newman and Heinselman 2012; Xu et al. 2015). Strengthening mesovortices above the ground can lead to an upward-directed vertical pressure perturbation gradient force, which in turn enhances low-level updrafts and strengthens the initial mesovortices. This mechanism may be responsible for the intensification of mesovortices that are located near an RIJ (e.g., Xu et al. 2015) and, in some cases, the potential for a mesovortex to produce a tornado (Atkins et al. 2005).

b. *Tornadoes in QLCSs*

While nearly all violent (EF4–5) tornadoes are spawned by supercells, it is estimated that 18% of all tornadoes are associated with QLCSs (Trapp et al. 2005). Given the propensity of QLCSs to persist overnight, these tornadoes are more likely to occur in the late night and early morning hours than supercellular tornadoes (Trapp et al. 2005). This characteristic, in combination with lead times limited to an average of 5 min (Trapp et al. 1999), can render QLCS tornadoes just as dangerous to the public as their supercellular counterparts (Ashley 2007; Ashley et al. 2008). Thus, the investigation of low-level processes influencing tornadogenesis in QLCSs remains an important area of research.

As in the case of supercellular tornadoes, QLCS tornadogenesis appears to be directly related to the presence of a low-level mesovortex. Atkins et al. (2004, 2005) found all tornadoes in two damaging Midwest derechos to be associated with low-level mesovortices. These mesovortices were stronger, deeper, and lasted twice as long as nontornadic mesovortices; this is an intriguing finding, as supercellular mesocyclones that produce tornadoes may not differ significantly from those that do not (Atkins et al. 2004). Atkins et al. (2005) also concluded that the

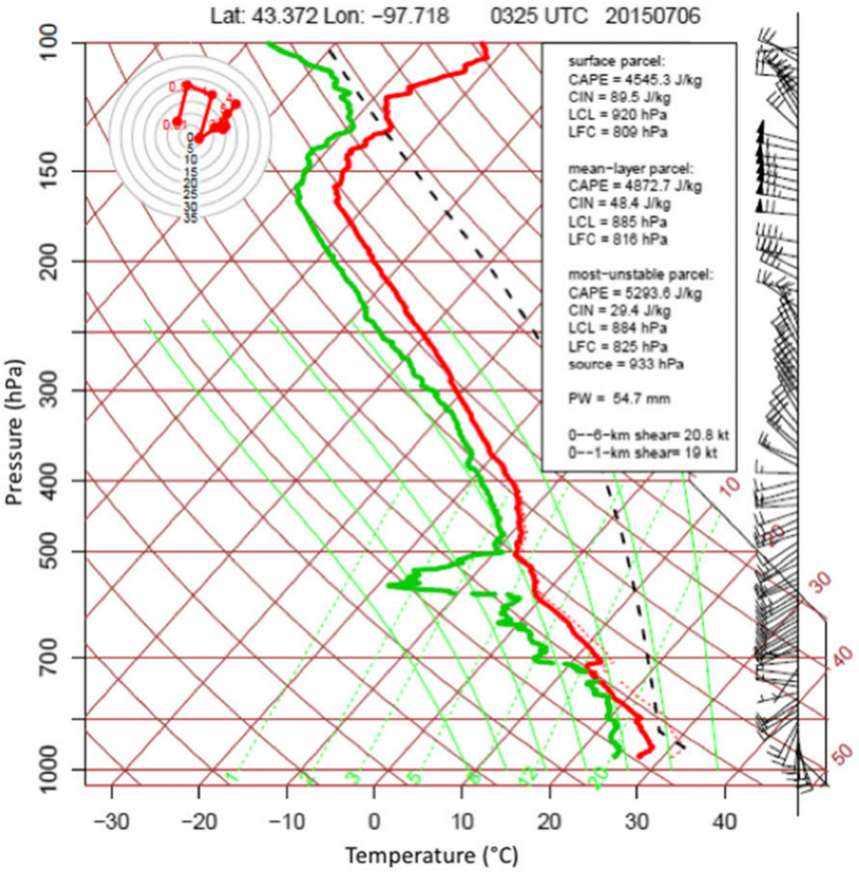

FIG. 4. Skew T–log$p$ diagram and 0–6-km hodograph (kt in upper left) from a radiosonde launched at 0325 UTC 6 Jul 2015 at the location of the star in Fig. 5. The dashed red line is the virtual temperature, and the black dashed line is the virtual temperature of the most unstable parcel. Variables computed from three different parcels are shown in the upper right.

stronger mesovortices associated with tornadoes may have been forced by a descending RIJ (e.g., Schaumann and Przybylinski 2012; Xu et al. 2015).

The present study provides an examination of the processes leading to mesovortex genesis and tornadogenesis in a QLCS that occurred on 6 July 2015 during the Plains Elevated Convection at Night (PECAN) field experiment. The next section features an overview of the synoptic conditions during the event as well as the PECAN assets that were deployed that night, followed by a description of the configuration used for the simulation of the mesovortex. Simulation results related to mesovortex development are described in section 4, followed by conclusions and discussions in section 5.

2. The 6 July 2015 PECAN case

a. Synoptic overview

At 0000 UTC 6 July 2015, weak midlevel westerly flow was present over the Rockies while a 50–60-kt (1 kt $\approx 0.5144\ \mathrm{m\ s^{-1}}$) jet moved through Manitoba and Ontario (Fig. 2). Northwesterly, 500-hPa flow of 15–20 kt over southeastern South Dakota transitioned to 20–30-kt westerly flow during the next 6 h (not shown) as a trough moved eastward into the Dakotas. A surface front stretched from western South Dakota to a broad region of low pressure east of the Front Range of the Rockies (Fig. 3). The southerly and southeasterly flow east of this low-pressure area advected warm, moist air northward into South Dakota with temperatures nearing 90°F and dewpoints above 70°F. Even though average midlevel lapse rates were only 6°–7°C $\mathrm{km^{-1}}$ (not shown), this warm, moist boundary layer supported most unstable convective available potential energy values above 5000 J $\mathrm{kg^{-1}}$ (see Fig. 4). Although the deep-layer vertical wind shear was relatively weak (20–30 kt over the lowest 4–6 km AGL; Fig. 4), it was sufficient to support loosely organized multicell convection capable of damaging wind gusts and hail. However, low-level winds strengthened, and storm-relative helicity

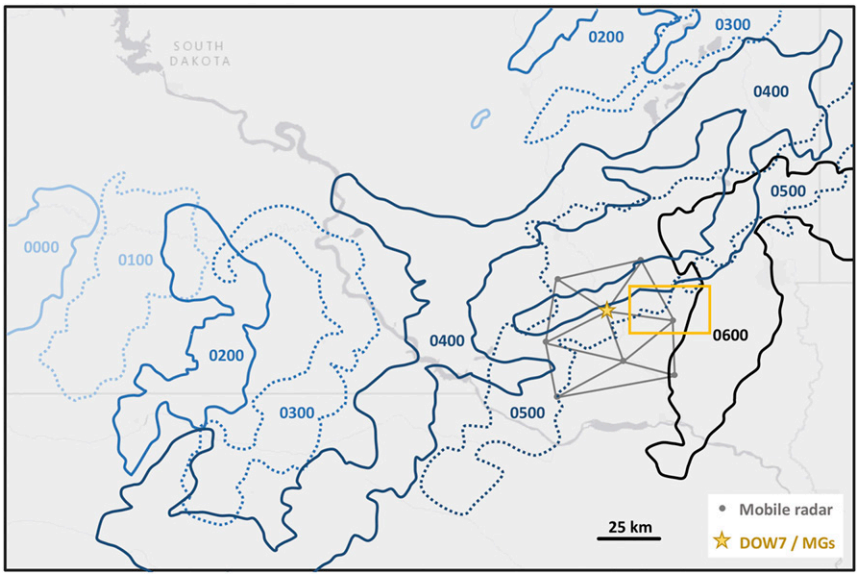

FIG. 5. Hourly composite of 40-dB*Z* reflectivity contours from 0000 to 0600 UTC 6 Jul 2015 from the NSSL Multi-Radar Multi-Sensor System. The final locations of eight mobile radars and baselines between them (30–50 km) are shown in gray. The star represents the location from which a sounding was launched from at 0325 UTC (see Fig. 8), and the gold box indicates the zoomed-in view of Fig. 6.

increased in the lowest 1.5 km AGL (Fig. 4) prior to the arrival of convection in the PECAN domain (Fig. 5), supporting more robust, rotating updrafts and a risk for the development of low-level mesovortices and associated tornadoes.

b. PECAN field deployment

The field phase of PECAN occurred from 1 June to 15 July 2015 with the goal of furthering our understanding of continental, nocturnal, warm-season precipitation. This overarching goal included specific foci on four atmospheric phenomena that included mesoscale convective systems (MCSs). During the evening of 5 July, PECAN assets were deployed ahead of an MCS that developed over south-central South Dakota around 0000 UTC 6 July (Bodine and Rasmussen 2017) and moved through the PECAN observing network over southeast South Dakota (Fig. 5). A pair of cyclonic mesovortices formed over the northeast portion of the network (Fig. 6), with the northern mesovortex becoming much stronger and producing an EF-0 tornado.

Three collocated mobile radiosonde systems staggered the release of radiosondes such that vertical profiles were obtained approximately every 20 min as the MCS approached (their location is indicated by the star in Fig. 5). Separate mobile profiling systems were deployed at other locations in the network and collected continuous data from a variety of remote sensing systems while releasing radiosondes every hour. Three aircraft collected both in situ and microphysical data during the deployment ahead of the convective lines and along spiral ascents/descents within the trailing stratiform precipitation. Other fixed observing sites across Kansas and Nebraska released radiosondes at 3-h intervals. A subset of these data was assimilated into an ensemble analysis and forecasting system (described in section 3) including in situ data from two aircraft, data from six mobile radars, three WSR-88Ds, and radiosondes. Interested readers are referred to Geerts et al. (2017) for details of these PECAN observing systems.

3. Numerical simulation configuration

A predecessor system that has since evolved into the NSSL Experimental Warn-on-Forecast (WoF) System for ensembles (NEWS-e; Wheatley et al. 2015; Jones et al. 2016; Lawson et al. 2018) was used for simulating the 5–6 July 2015 MCS. This system assimilates observations using an ensemble Kalman filter (EnKF; Evensen 1994) into an ensemble of model states created by WRF-ARW version 3.6.1 (Skamarock and Klemp 2008) using the Data Assimilation Research Testbed (Anderson et al. 2009). The ensemble has 36 members that are created by using different parameterization schemes for longwave and shortwave radiation, the surface layer for heat, moisture, and momentum fluxes, and turbulent mixing in

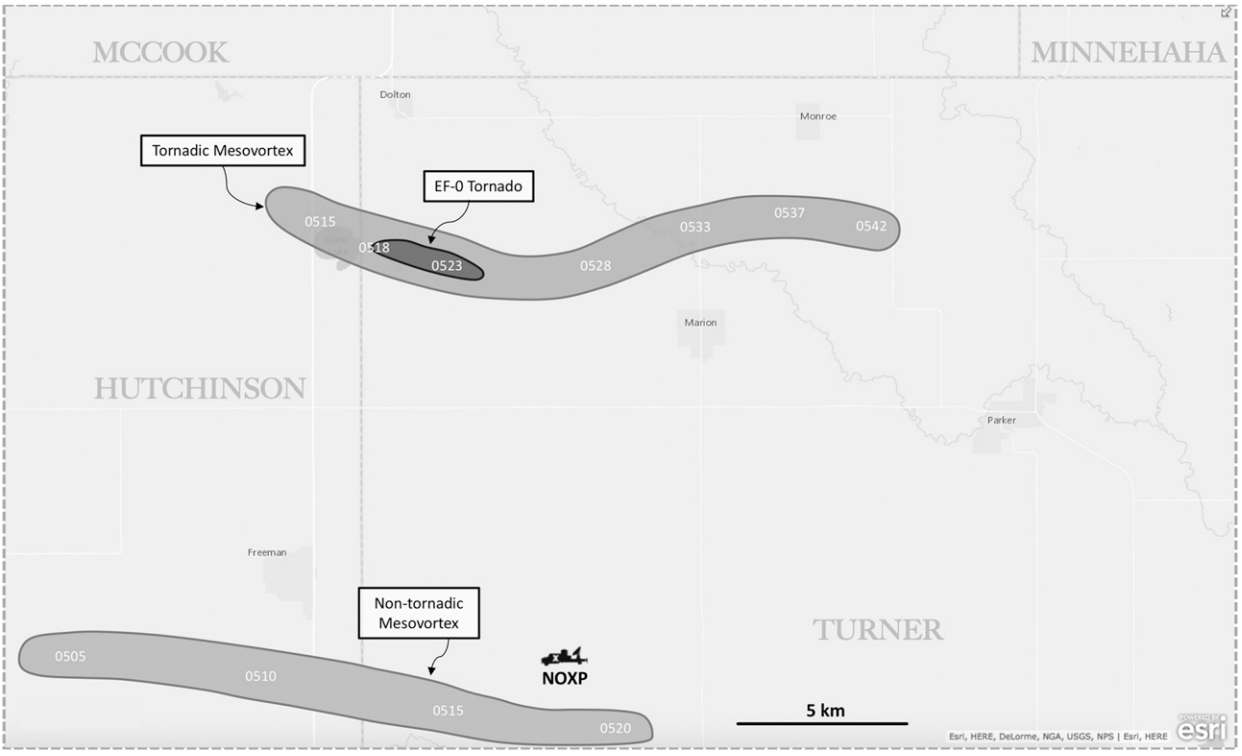

FIG. 6. Schematic showing the paths of the two observed low-level mesovortices, EF-0 tornado, and NOXP. The observed mesovortices locations were determined using mobile and WSR-88D radar observations from Sioux Falls, SD.

the planetary boundary layer (PBL), as well as by using the initial conditions provided by 18 members of the Global Ensemble Forecast System [GEFS; the configuration is the same as that detailed by Hitchcock et al. (2016)]. Please reference Wheatley et al. (2015) for a full description of the physics options used for the first 18 GEFS members (see their Table 2). For members 19–36, these physics options are applied in reverse order (i.e., member 19 is constructed by applying physics option 1 to GEFS member 18, etc.) such that no member is identically configured. The Thompson microphysics scheme including six classes of moisture species and ice number concentration as prognostic variables was used in all members (Thompson et al. 2004); the microphysics scheme was not perturbed between members. A total of 51 vertical levels were used, with the spacing varying from 25 m near the surface to near 780 m at the model top (50 hPa). Eight vertical levels were located in the lowest 1 km AGL.

A series of four nested grids was used, with the three inner grids nested one way with their outer grid (Fig. 7). Horizontal grid spacings were 15 km, 3 km, 1 km, and 333 m. The ensemble state was initialized by interpolating the GEFS analyses valid 1800 UTC 4 July to the 15-km grid and was integrated in WRF-ARW for 6 h before 24 data assimilation cycles from 0000 to 2300 UTC 5 July (Fig. 8). These hourly assimilation cycles included conventional observations from the Meteorological Assimilation Data Ingest System (MADIS; Miller et al. 2007) and PECAN radiosondes. The MADIS observations include (i) mandatory and significant levels from NWS radiosondes; (ii) surface data from routine aviation weather

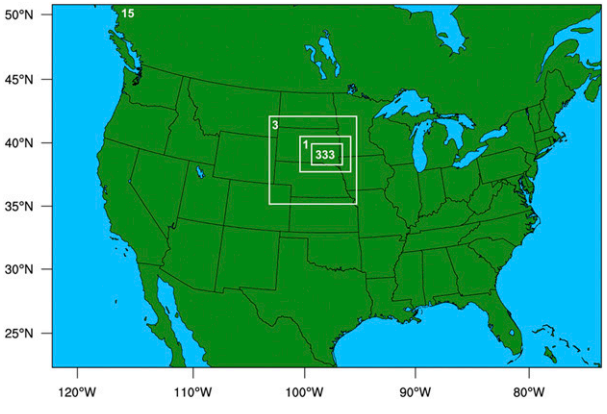

FIG. 7. Domain configuration for the simulations. The domains are labeled by their horizontal grid spacings (15 km, 3 km, 1 km, and 333 m).

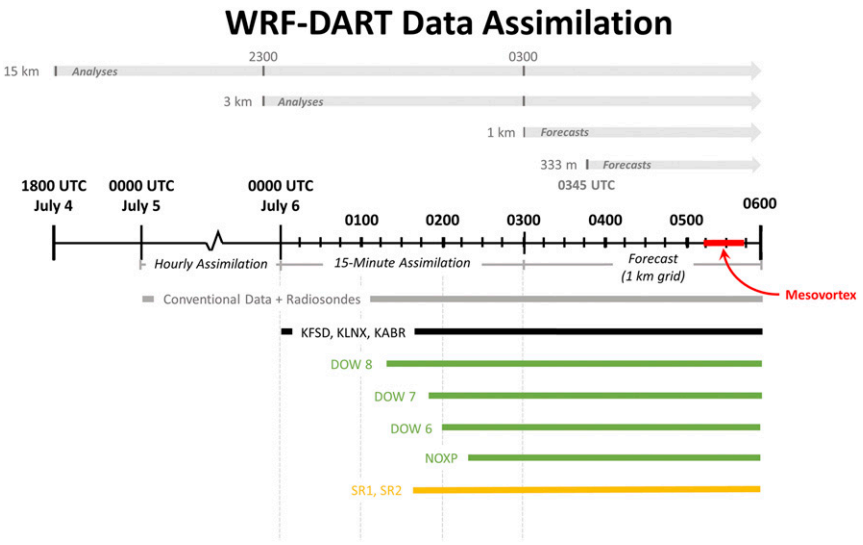

FIG. 8. Synthesis of the data assimilation for this ensemble simulation. Analyses and forecasts produced on each grid are shown above the black timeline, and time periods in which the data from each platform were used in the 15-min assimilation windows are shown below the black timeline. The three WSR-88D radars included Sioux Falls (KFSD), North Platte (KLNX), and Aberdeen (KABR). The six mobile radars included three Doppler on Wheels, two Shared Mobile Atmospheric Research and Teaching Radars, and NOAA X-band Polarimetric Radar.

reports (METARs), marine reports (from both ships and buoys), the Oklahoma Mesonet, and mesonet observations from a variety of national networks; (iii) Aircraft Meteorological Data Relay (AMDAR) reports for wind and temperature; and (iv) atmospheric motion vectors derived from satellite observations (as in Coniglio et al. 2016).

At 2300 UTC 5 July, the 3-km grid was initialized from the 15-km analysis and was integrated for 1 h. Assimilation on the 3-km grid was performed from 0000 to 0600 UTC 6 July every 15 min and included radiosonde observations, Doppler radial velocity (e.g., Snyder and Zhang 2003; Zhang et al. 2004), and reflectivity (e.g., Dowell et al. 2004; Tong and Xue 2005; Aksoy et al. 2009, 2010; Yussouf and Stensrud 2010; Dowell et al. 2011; Yussouf et al. 2013) from the mobile and WSR-88D radars listed in Fig. 8. All radar data were quality controlled and dealiased using Py-ART software (Helmus and Collis 2016) as well as subjectively using the Earth Observing Laboratory Solo3 software. The reflectivity and Doppler velocity data were then analyzed onto a 6-km grid with a two-pass Barnes scheme (Barnes 1964) using Observation Processing and Wind Synthesis (OPAWS) software before assimilation onto the 3-km grid. Standard errors of 5 dBZ and 2 m s^{-1} were assumed for the reflectivity and velocity observations, respectively, during the EnKF assimilation process, similar to many studies that assimilate Doppler radar observations (e.g., Yussouf et al. 2013). Radial velocity observations were only assimilated if reflectivity > 10 dBZ. The radiosonde observations were quality controlled and thinned to 50–60 vertical levels prior to assimilation. At 0300 UTC, the analysis on the 3-km grid was used to initialize the 1-km grid, and 1-km forecasts were generated out to 0600 UTC (using 3-km analyses for the

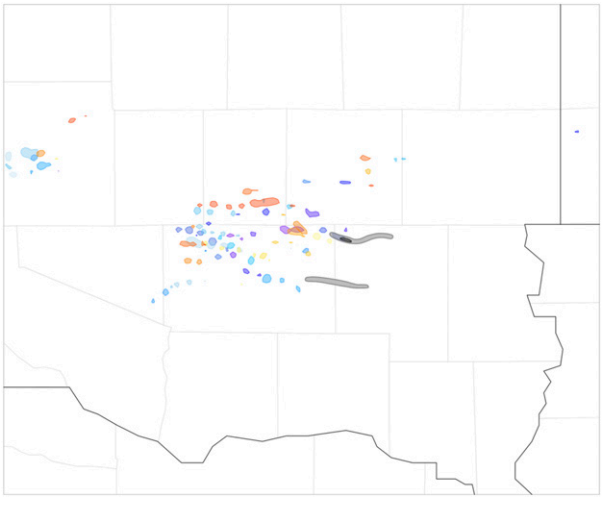

FIG. 9. Vertical vorticity swaths averaged in the lowest four model levels (approximately the lowest 150 m AGL) exceeding 0.01 s^{-1} from 0400 to 0600 UTC (1–3-h forecasts) at 5-min intervals for each ensemble member (indicated by the different colors). Observed mesovortices and the tornado track from Fig. 6 are overlaid.

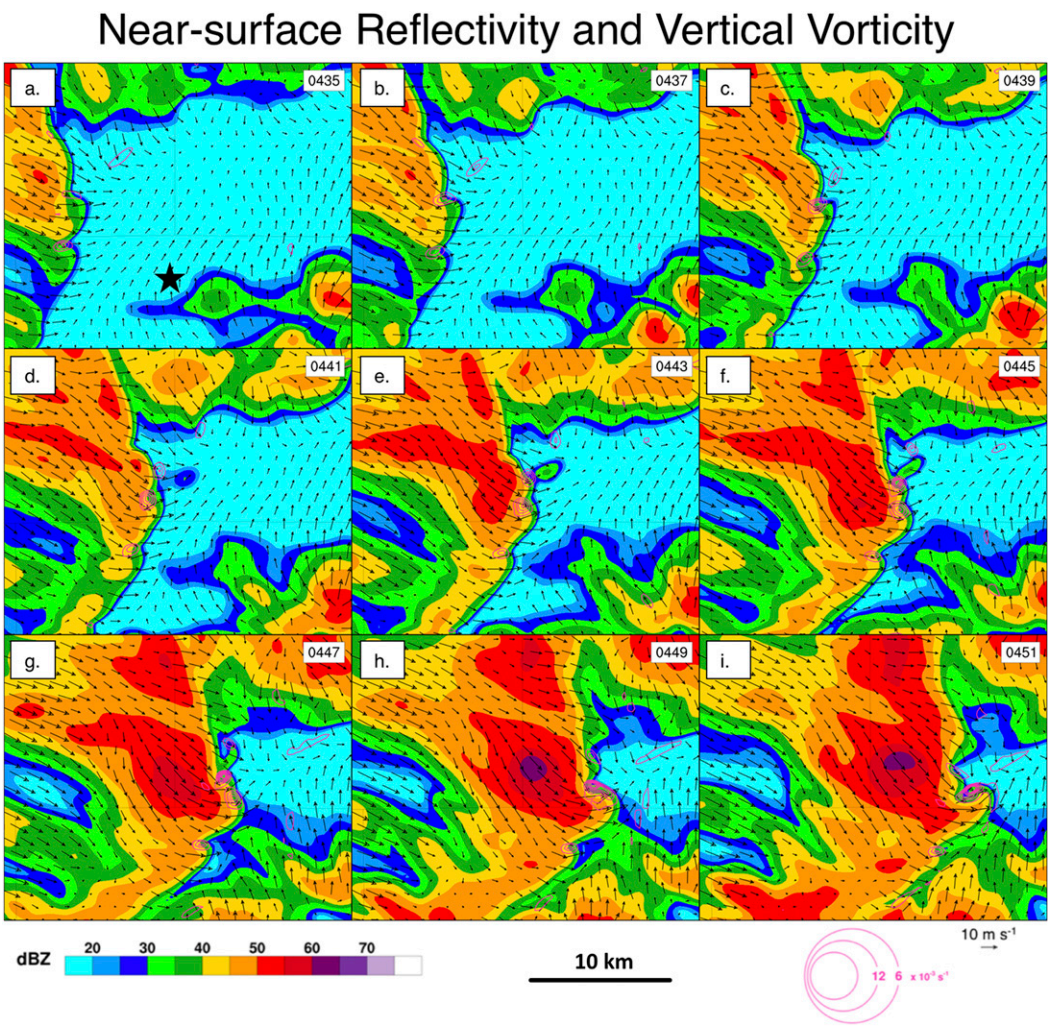

FIG. 10. Simulated lowest model-level reflectivity (scale in lower left), vertical vorticity (pink contours with scale in lower right), and ground-relative winds (scale in lower right) from member 30 from 0435 to 0451 UTC on the 333-m grid. (a) Black star represents the location that the simulated hodographs were extracted from in Fig. 13.

lateral boundary conditions). The 1-km forecasts valid at 0345 UTC from several ensemble members were then used as the initial and boundary conditions for forecasts on the 333-m grid at 0345 UTC.[2] Forecasts for these members were created through 0600 UTC 6 July on the 333-m grid.

[2] Tests were performed with data assimilated onto the 1-km grid every 5 min in an attempt to constrain the analyses on the 1-km grid further toward observations. However, forecasts generated from these 1-km analyses were inferior to those generated from the downscaled 3-km analyses, with too much spurious convection generated shortly after the forecasts were initialized (not shown). This is an ongoing research problem within storm-scale assimilation systems on grids $O(1)$ km (D. Wheatley 2016, personal communication).

4. Simulation results

a. Comparison to observations

All of the ensemble forecasts produce an MCS in their forecasts with a general evolution similar to the observed evolution of the system. In addition to simulating the general structure of the MCS, many of the 1-km forecasts produce mesovortices of varying intensity and longevity (Fig. 9). When compared to the observed mesovortex tracks (Fig. 9), the ensemble forecasts contain significant low-level rotation about 20–30 km west of the observed tornadic and nontornadic mesovortices. Inspection of the ensemble forecasts' evolution of the MCS shows that this is the result of the system evolving faster than in nature. However, careful analysis of storm-scale features reveals many similarities between the 333-m forecasts and

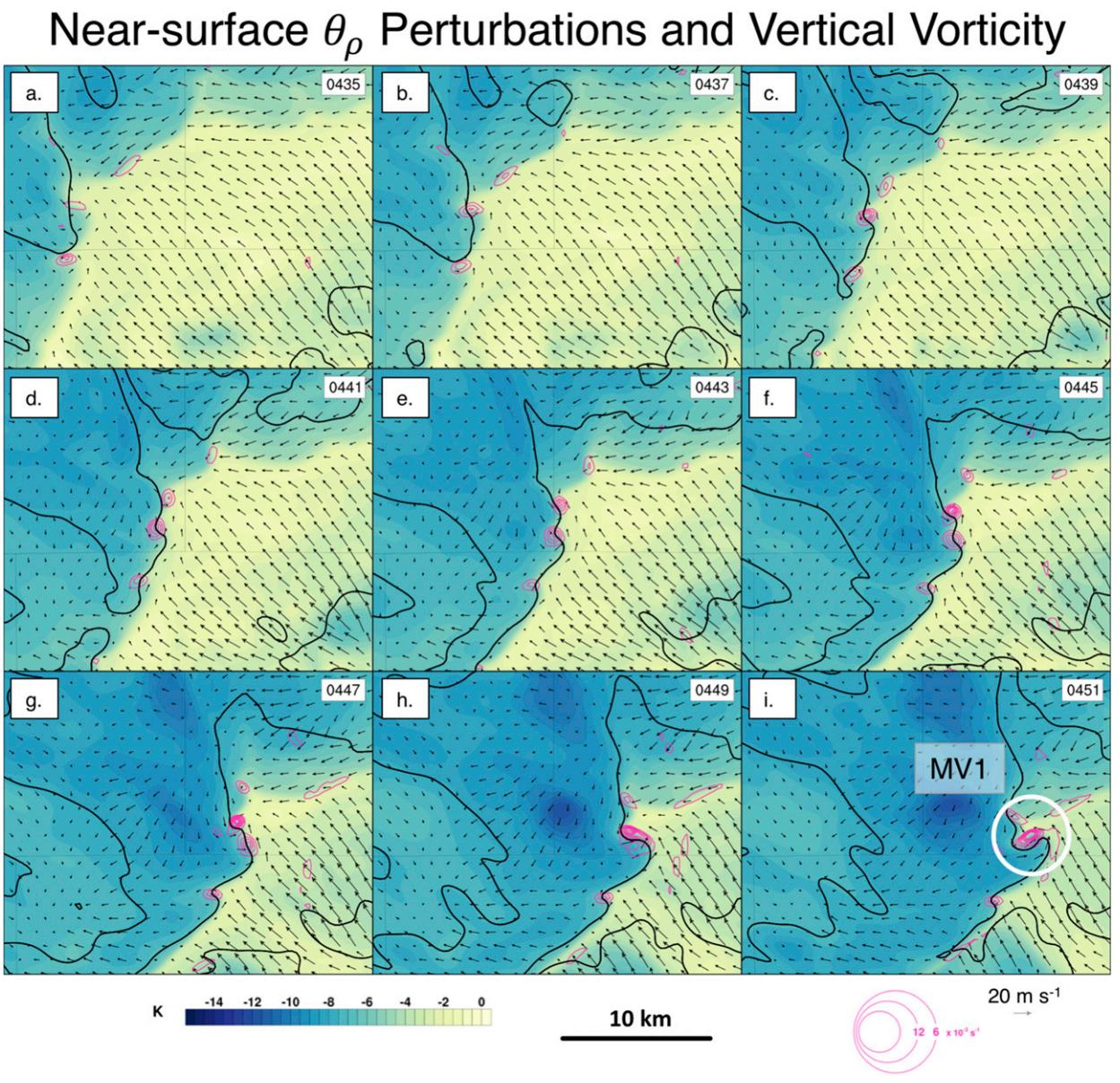

FIG. 11. As in Fig. 10, but for lowest model-level density potential temperature (θ_ρ), perturbations (shaded), and storm-relative winds. (i) The MV that is the subject of this study is labeled as MV1.

observations in the development of the mesovortices. This is especially true for member 30, as detailed below. Parameterizations for this specific member included the Rapid Radiative Transfer Model for general circulation models (RRTMG) longwave and shortwave radiation schemes, RUC surface physics, MYNN surface-layer physics, and a 3D TKE turbulent diffusion scheme (no planetary boundary layer scheme was used).

A complex storm-scale evolution is evident in member 30 forecasts valid from 0435 to 0455 UTC (Fig. 10). Outflow generated by convective downdrafts (e.g., over the lower-right portion of the panels in Fig. 10) is evident ahead of the main east-southeastward-moving MCS (Figs. 10 and 11). Convection was similarly observed to develop ahead of the main system (Figs. 12a,c). The forecasts also contain a west-southwest–east-northeast-oriented band of convection to the north and east of the main MCS, seen moving to the south from the upper part of the panels in Fig. 10. A west-southwest–east-northeast-oriented band of convection with a well-defined gust front also was observed (Fig. 12a) that moved steadily to the south and east (Fig. 12c).

Southeasterly mesovortex-relative near-surface winds of 15–20 m s^{-1} were present ahead of the gust front

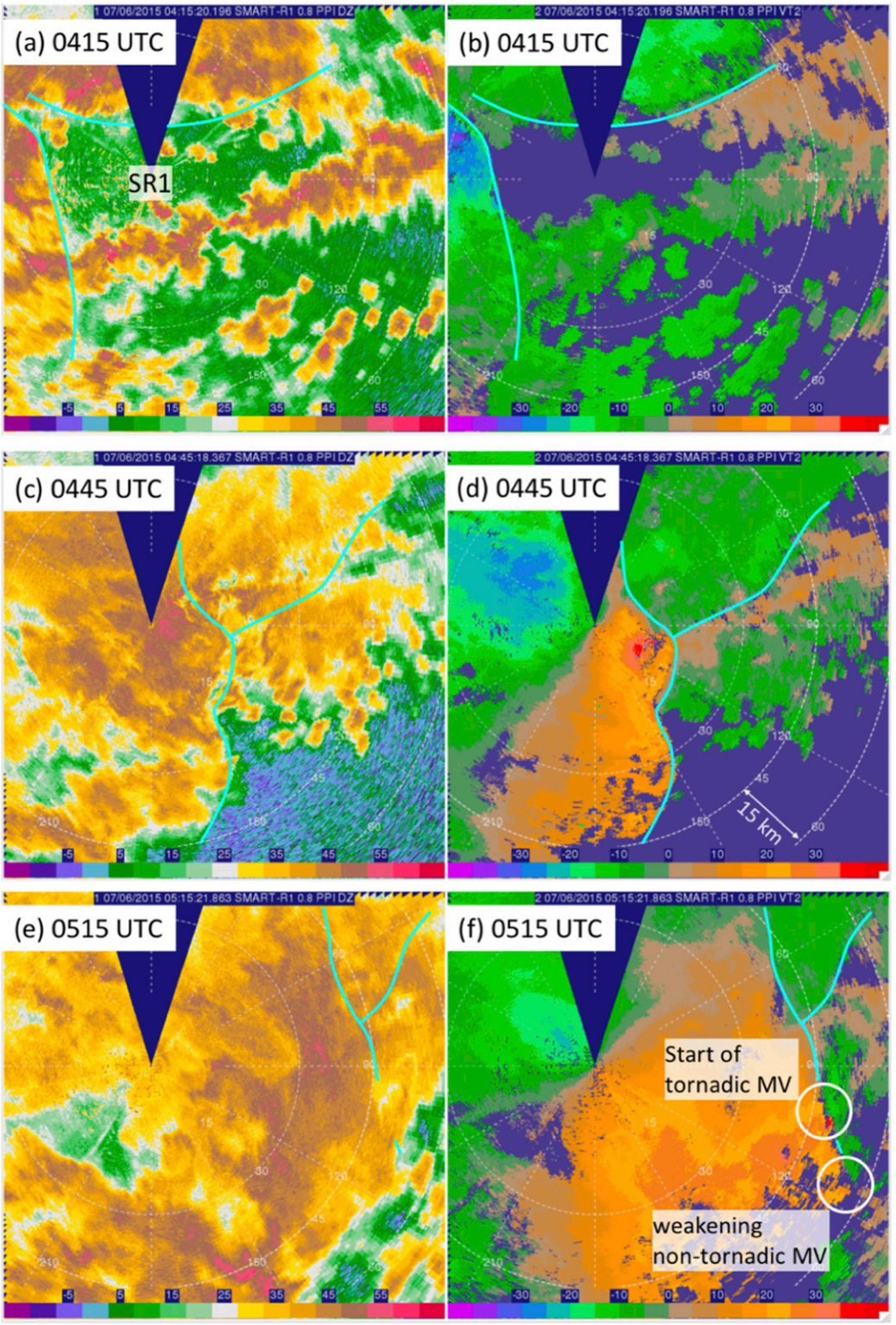

FIG. 12. (a),(c),(e) Reflectivity (dBZ) and (b),(d),(f) radial velocity ($m\,s^{-1}$) observations from SR1 (location shown in uppermost left panel) at a scanning elevation of 0.5° at 0415, 0445, and 0515 UTC. Approximate locations of the two gust fronts described in the text are indicated by the blue lines. The tornadic and nontornadic mesovortices at 0515 UTC are labeled and circled in the lowermost right panel. The horizontal scale is shown in (d).

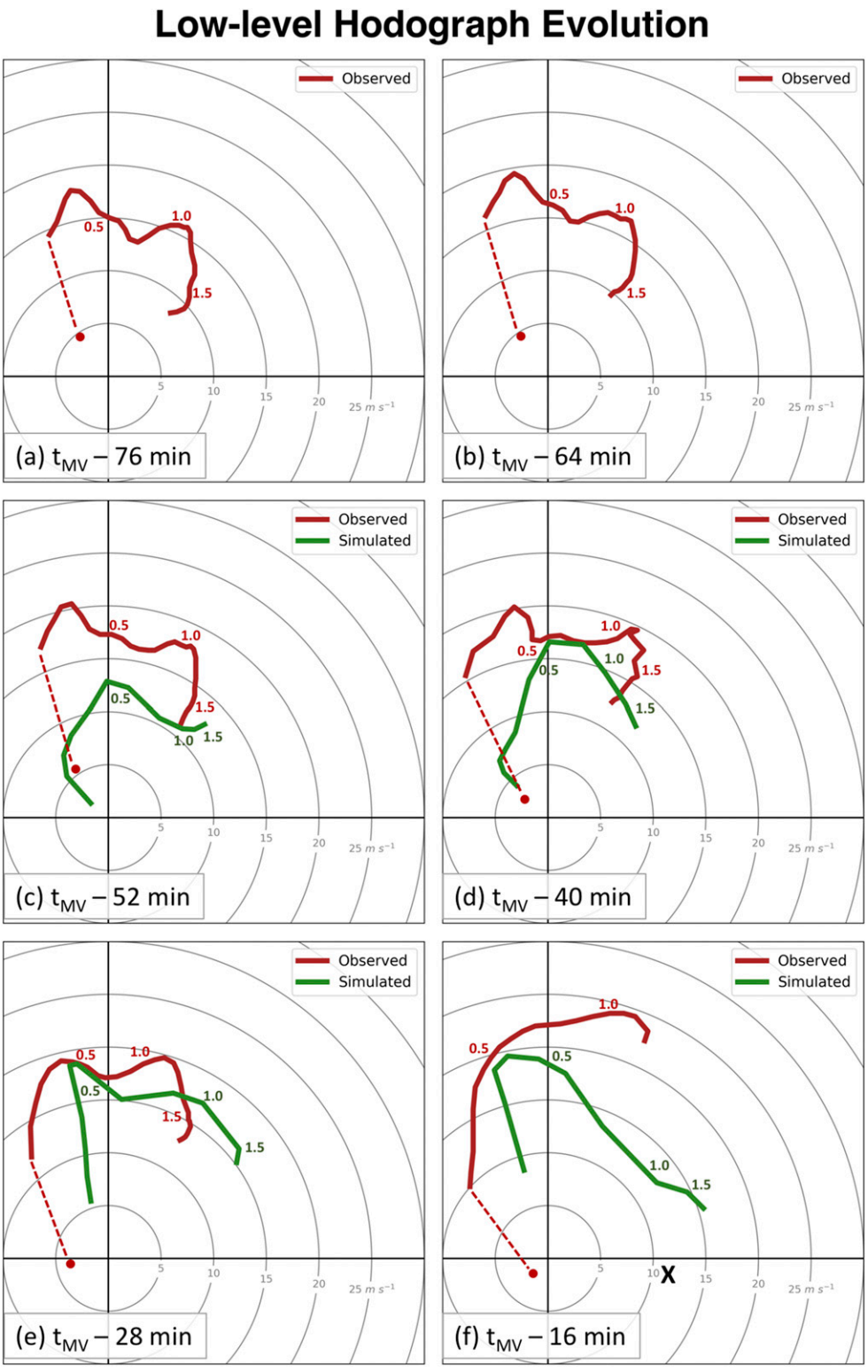

FIG. 13. Evolution of both observed and simulated low-level hodographs every 12 min from 76 to 16 min prior to the time the MV passed by the Collaborative Lower-Atmospheric Mobile Profiling System (CLAMPS) for the ''observed'' hodographs (0510 UTC) or the time of maximum near-surface (i.e., lowest model level) vertical vorticity associated with the mesovortices for the ''simulated'' hodographs (0447 UTC). (a)–(f) Observed hodographs plotted from 0354 to 0454 UTC and retrieved from a Doppler

(Fig. 11) because of a combination of strong larger-scale ground-relative near-surface winds (Fig. 10) combined with the motion of the system of approximately 12.5 m s^{-1} at 290°. The outflow ahead of the main MCS did little to modify the near-surface thermodynamic state (Fig. 11) but did enhance the near-surface wind speeds and backed the winds to a more southerly direction. This added to the already substantial low-level vertical wind shear in the simulated environment that was oriented nearly parallel to the gust front (Fig. 13), which is consistent with observations from velocity–azimuth display wind retrievals from a Doppler wind lidar obtained in the region ahead of the main system in the enhanced southerly winds.

The observed tornadic mesovortex (and the strongest mesovortex in the forecasts, labeled as MV1 in Fig. 11i) both occur near (within 20 km of) the interface of the gust fronts associated with the main MCS and the west-southwest–east-northeast-oriented band, as well as in the vicinity of the convection that developed ahead of the main MCS. A zoomed-in view of the evolution of MV1 in the simulation is shown in Fig. 14. What developed into a single mesovortex by ~0449 UTC (Fig. 11i) formed from a merger of two smaller mesovortices (labeled MV1a and MV1b in Fig. 14c). The cyclonic vertical vorticity within MV1a develops along the western edge of the west-southwest–east-northeast gust front and slowly strengthens as it nears the main MCS gust front. MV1b develops on the gust front of the main MCS and is associated with the strong localized rear-inflow surge located just to its west (Fig. 10). It is also important to note the development of a persistent anticyclone just to the west of MV1a (Figs. 14c–g).

While there was not clear evidence from any of the PECAN mobile radars that the observed tornadic mesovortex resulted from a merger of two mesovortices,[3] radial velocity observations available every 5 min from Sioux Falls, South Dakota (KFSD), suggest that two separate mesovortices may have merged to form the single tornadic mesovortex observed at 0525 UTC (Fig. 15). While 5-min intervals from KFSD are not frequent enough to deduce mesovortex evolution/mergers and make a clear determination of which mesovortex observed at 0520 UTC (Fig. 15d) becomes the tornadic mesovortex observed at 0525 UTC (Fig. 15f), it appears that the more northern of the two mesovortices at 0520 UTC intensifies rapidly and ingests the southern mesovortex by 0525 UTC. This is qualitatively very similar to what occurs in the simulation (Fig. 14), as the more northern of the two observed mesovortices forms near the west-southwest–east-northeast-oriented gust front, and the southern observed mesovortex forms along the north side of the leading edge of the strong rear-inflow surge (Figs. 15a,b). Although the simulated near-surface winds do not attain tornadic intensity in the vicinity of MV1 (e.g., Fig. 10), the storm-scale similarities of the observed mesovortex to the simulated mesovortex near the location of the merging gust fronts and along a rear-inflow surge justify examining the simulation further to deduce the processes involved in the development of the tornadic mesovortex.

b. *Analysis of the simulated mesovortex*

To analyze the evolution of MV1 (Fig. 11i), air parcel trajectories [following an iterative method described by Seibert (1993)] were initialized at 0435 UTC in a volume centered on the path of the developing mesovortex and integrated forward in time for 20 min. Parcels were initially spaced every 500 m over a 50 km × 50 km area, with parcels every 100 m in the vertical from 100 to 2500 m AGL, yielding 255 025 parcels total. Model output every 5 s was used to compute the trajectories as well as vertical vorticity, vertical vorticity tendency terms, and other meteorological quantities along the trajectories. Parcels that contributed to the development of MV1 at any given time were defined using a few

[3] The mobile X-band radars were attenuated by the abundant convective precipitation, and the mesovortex was at the edge of the range of the C-band SR1 and SR2 radars at this time.

←

wind lidar on the CLAMPS (see Geerts et al. 2017). The profiles are smoothed lightly in time and height using a Gaussian filter to remove small-scale noise. The DWL profiles begin at 113 m AGL because of limitations of the lidar in sampling the near field and because of the light smoothing applied. However, the observed wind profile is extrapolated down to approximately 2 m AGL (red dashed line) using the wind observation from the mobile mesonet closest to CLAMPS at the specified time (red circle). The MCS gust front passed the CLAMPS location at about 0510 UTC, 16 min after the hodograph shown in the last panel. Simulated hodographs were extracted at the location indicated in Fig. 10a every 12 min from 0355 to 0431 UTC. Simulated hodographs are not shown in (a),(b) because forecasts on the 333-m grid began at 0345 UTC. Heights AGL (km) are indicated along each hodograph, and the "×" in the last panel represents the observed MV motion.

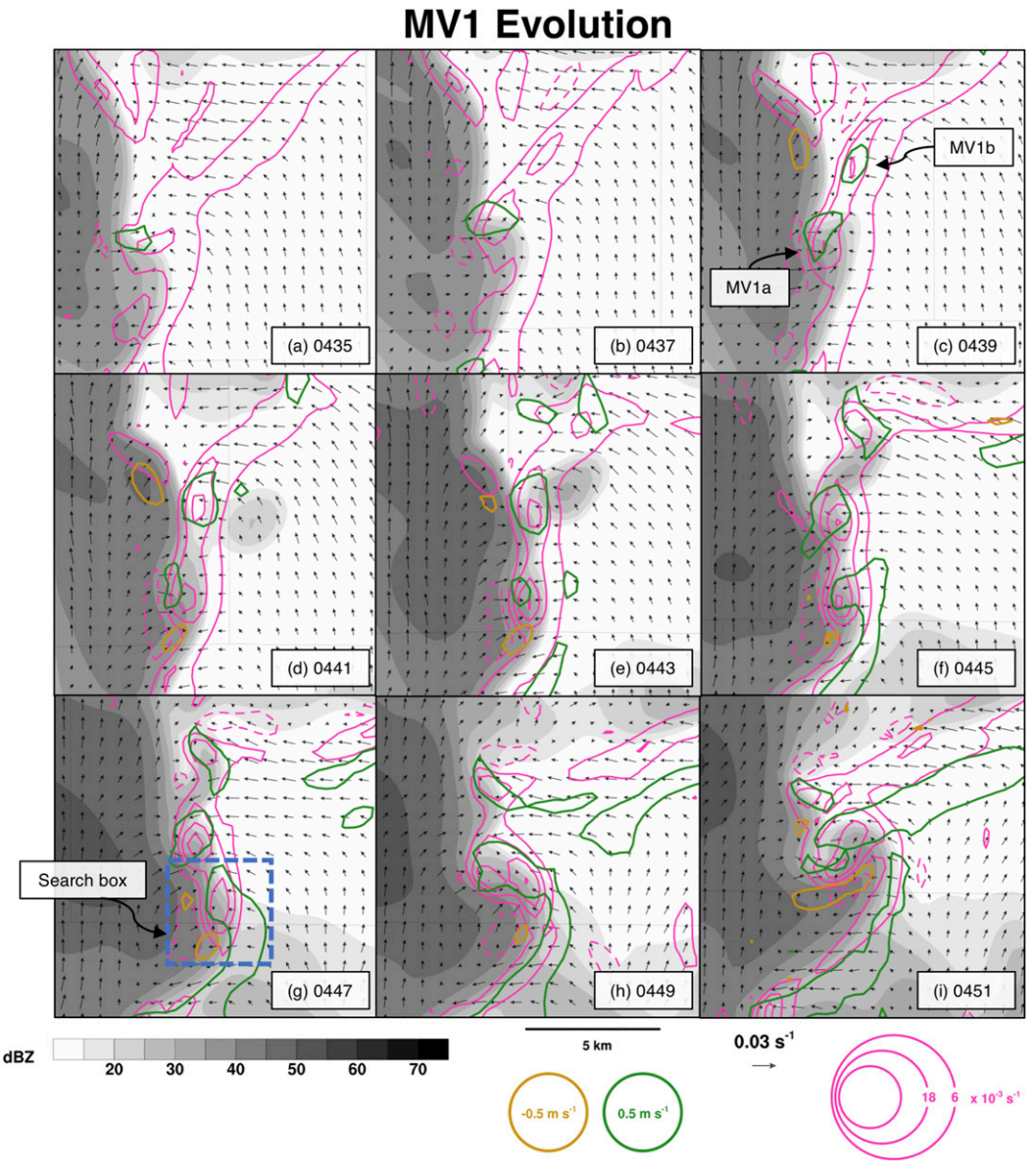

FIG. 14. Zoomed-in view following the evolution of what becomes MV1 (see Fig. 11i) with 1-km AGL vertical vorticity (pink contours), 500-m horizontal vorticity (arrows), and 500-m AGL vertical velocity $>0.5\,m\,s^{-1}$ ($<-0.5\,m\,s^{-1}$; green/brown contours). Positive vertical vorticity contours are solid, and negative vertical vorticity contours are dashed. The two mesovortices that merge to form MV1 are labeled as MV1a and MV1b in (c). Valid times in UTC are indicated in the lower right of each panel. The 4-km-wide search box used at 0447 UTC is shown, but for the sake of clarity is not shown at other times.

constraints. A 4-km-wide search box (Fig. 14g) centered on MV1a (labeled in Fig. 14c) over time was used, as well as a vertical velocity threshold of $1\,m\,s^{-1}$, a vertical vorticity threshold of $0.006\,s^{-1}$ (i.e., the first pink contour in Figs. 10 and 11), and a height threshold of 250–2000 m AGL. The box was centered on MV1a since this mesovortex intensified more rapidly than MV1b in the time period examined and was associated with a stronger updraft throughout the intensification period (Fig. 14).

Using the above method, approximately 60–80 parcels were found to be in the mesovortex at any time. The median, 90th percentile, and 10th percentile vertical velocities and vertical vorticities of parcels located within the mesovortex at each time step are shown in Fig. 16. The median vertical velocity of the parcels within the mesovortex rapidly increased from 0435 to 0440 UTC along with a gradual increase in median vertical vorticity. For the next 10 min, the median

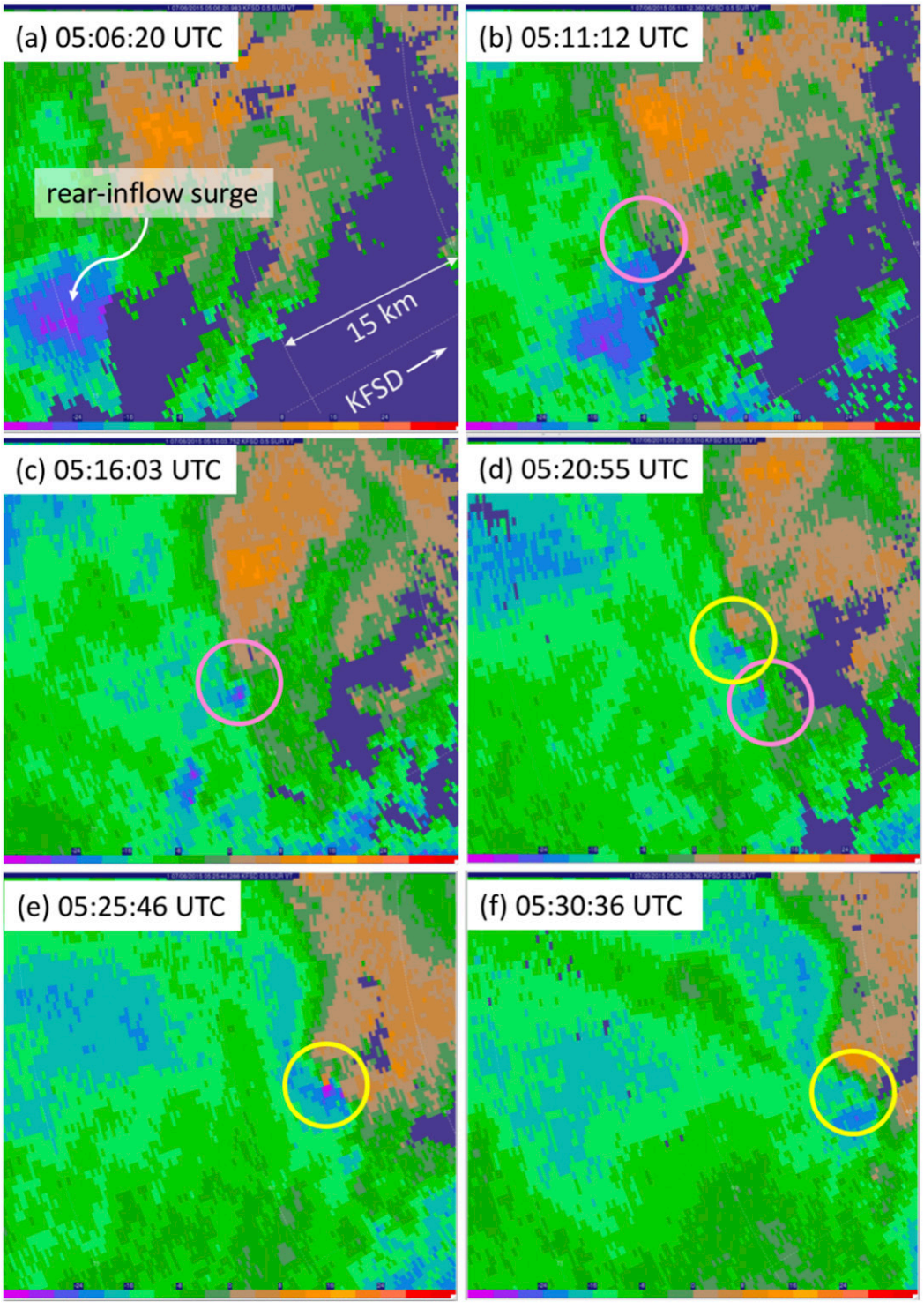

FIG. 15. Radial velocity observations ($m\,s^{-1}$; scale at the bottom of each panel) from KFSD (relative direction shown in the upper-left panel) approximately every 5 min from 0506 to 0530 UTC at approximately 500 m AGL. The rear-inflow surge discussed in the text is highlighted in the upper-left panel. The two mesovortices that merge to form the single, observed, tornadic mesovortices are circled in pink and yellow.

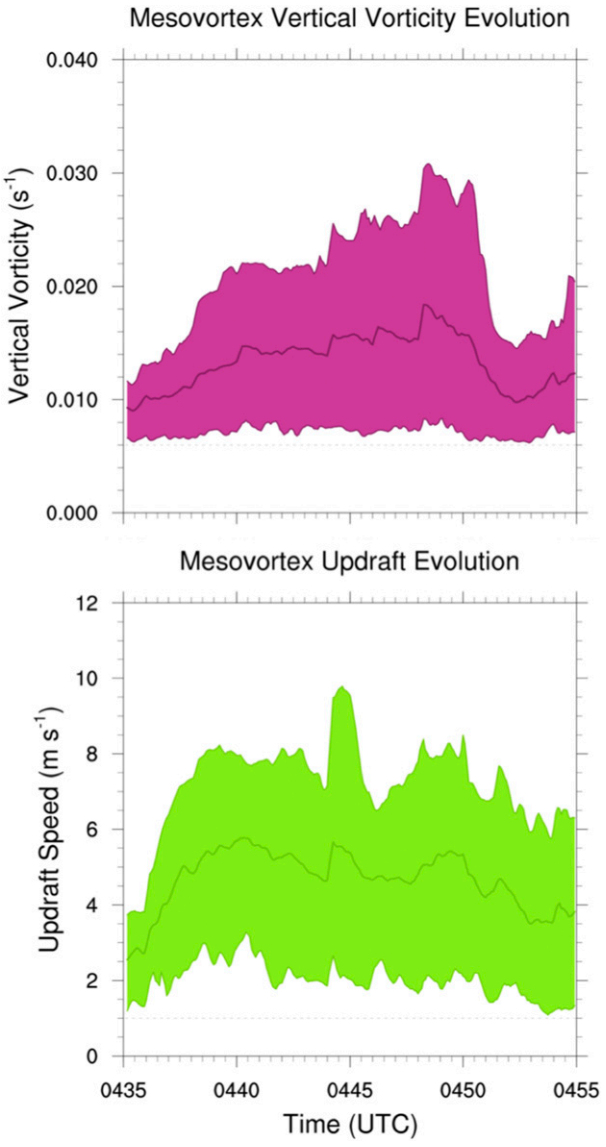

FIG. 16. Median, 10th, and 90th percentiles of (top) vertical vorticity and (bottom) updraft speed for parcels located in the mesovortices from 0435 to 0455 UTC. The vertical vorticity and updraft thresholds used to determine if a parcel was located in the mesovortices at a given time are marked with a dashed, gray line in each plot. In total, 60–80 parcels were located in the mesovortices at any given time from 0435 to 0455 UTC.

vertical vorticity in the mesovortex continued to gradually increase while the median vertical velocity fluctuated around $5\,m\,s^{-1}$. The median vertical velocity and vertical vorticity were strongest from 0447 to 0449 UTC, with a median updraft speed near $5\,m\,s^{-1}$ and vertical vorticity approaching $0.02\,s^{-1}$. This occurred at the same time as vertical vorticity values at the surface peaked and as the pair of mesovortices merged (Fig. 14). After 0450 UTC, the mesovortex decayed as vertical velocity and vorticity both decreased over the next few minutes.

Parcels that are in the mesovortex from 0441 to 0447 UTC originated from multiple source regions including the environment and storm-cooled air behind the gust fronts. Parcels originating in the environment (referred to as the *environmental* source region) resided close to the surface (100–300 m AGL) and had little vertical vorticity before reaching the gust front and low-level mesovortex updraft (Fig. 17). These parcels rose within the forced updraft along the gust front as they flowed poleward and were then pushed eastward by the leading edge of the main MCS cold pool. These parcels gradually attained higher vertical vorticity values during this period (shown by the thickening lines in Fig. 17) before rising more rapidly upon encountering the low-level updraft associated with the mesovortex. This process occurred throughout the entire intensification stage of the mesovortex. A second source region behind the west-southwest–east-northeast-oriented gust front is evident north of the mesovortex (henceforth deemed the *northern* source region). Parcels from this source region originated at low levels and gradually attained more vertical vorticity and ascended as they approached the developing mesovortex (Fig. 18). The parcels then rose rapidly upon encountering the mesovortex low-level updraft. The third source region originated well to the northwest of the developing mesovortex and was associated with a localized downdraft/rear-inflow jet (henceforth deemed the RIJ source region). These parcels originated near 1 km AGL with larger initial cyclonic vertical vorticity than the parcels in the other source regions but descended before rising rapidly in the low-level mesovortex updraft (Fig. 19).

The development of vertical vorticity in the parcels from the environmental source region is examined further with composite time series of the streamwise and crosswise horizontal vorticity components (defined with respect to the storm-relative wind), along with the vertical vorticity tilting and stretching tendencies (Fig. 20). Integrated vertical vorticity along these environmental trajectories is very similar to interpolated vertical vorticity (Fig. 21), so that analyzing the evolution of vertical vorticity using the tendency terms is appropriate (the same is not true for the other source regions). The ''composite'' tilting and stretching terms were found by first calculating tilting and stretching for each individual parcel and then calculating the 10th, 50th, and 90th percentiles (as shown in Fig. 20). The parcel time series were then shifted in time such that the time of maximum stretching tendency (i.e., as the parcel encounters the low-level updraft) along each trajectory occurs at the

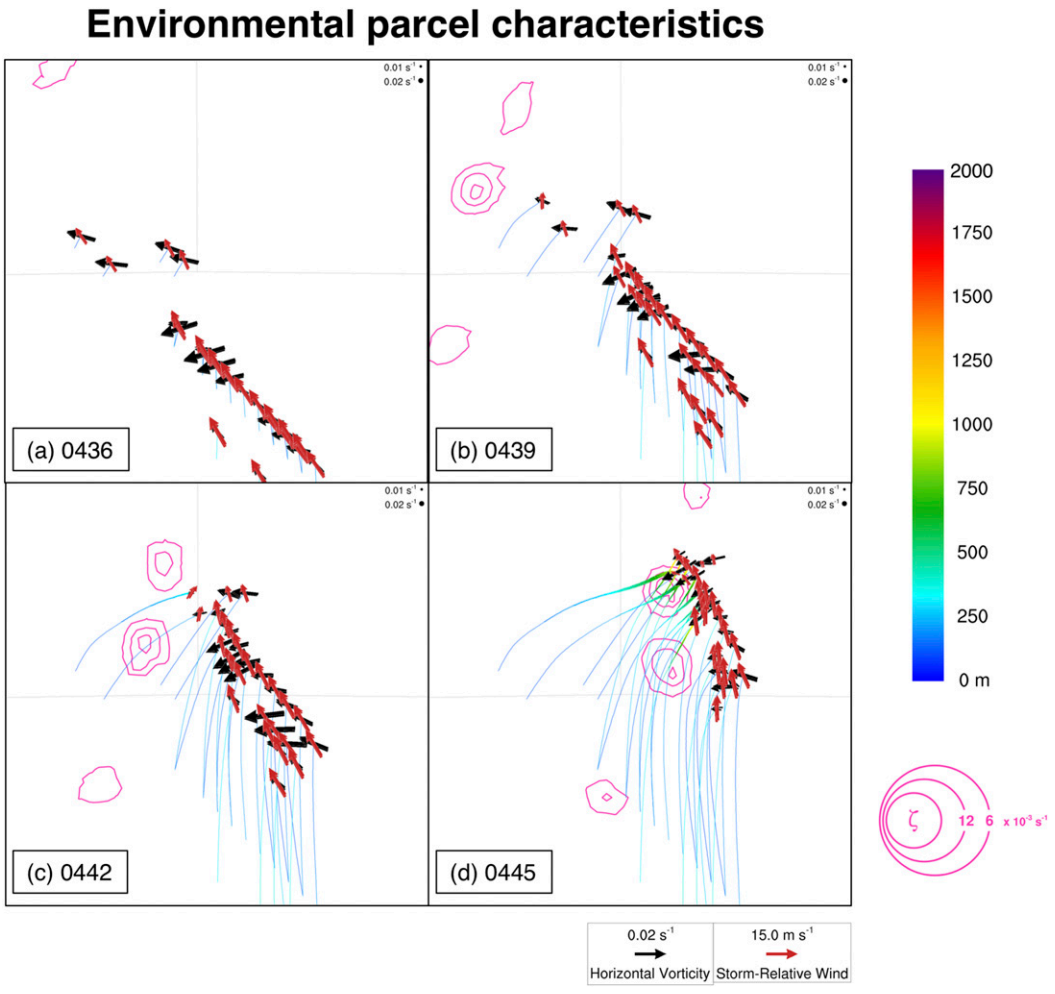

FIG. 17. Trajectory traces for an area zoomed in over the environmental parcels prior to their ingestion into the mesovortices updraft at 0447 UTC. The heights AGL of the parcels are indicated by their color (scale on the right), and the vertical vorticity of the parcels is indicated by their thickness (scale in the upper right of each panel). Red (black) arrows show the storm-relative wind (horizontal vorticity) at the parcel location at the time (UTC) indicated in the lower left of each panel (scales for the wind and horizontal vorticity are given in the lower right). Lowest model-level vertical vorticity is contoured in pink.

same time (defined as $t - 0$ in Fig. 20). The tilting and stretching terms appear rather intuitive as the parcels encounter the low-level mesovortex updraft, with the tilting term gradually increasing prior to a rapid increase in stretching and a subsequent gradual decrease in tilting as the horizontal vorticity is converted to cyclonic vertical vorticity. However, it is notable that the horizontal vorticity associated with these parcels was mostly *crosswise* prior to and during tilting, at least for the parcels located within the mesovortex at 0443–0447 UTC (Figs. 20b–d). This large crosswise vorticity is related to the large near-ground vertical wind shear oriented at a small angle to the gust front and storm-relative flow (Fig. 13). For parcels located within the mesovortex at 0445 and 0447 UTC, streamwise vorticity *decreases* and even becomes negative for some parcels prior to encountering the low-level mesovortex updraft.

Figure 20 shows that upward tilting of horizontal vorticity is the primary contributor to the *initial* generation of cyclonic vertical vorticity in the environmental parcels at low levels (2–4 min prior to their ingestion into the MV), followed by large stretching of vertical vorticity as the parcels enter the eastern periphery of the low-level updraft (0–2 min prior to their ingestion into the MV). Figure 17 shows this can be visualized as northward-flowing parcels with horizontal vorticity pointing westward that are tipped upward within the gust front updraft, resulting in cyclonic vertical vorticity. This process occurs prior to the parcels entering the updraft of the developing mesovortex. During this time,

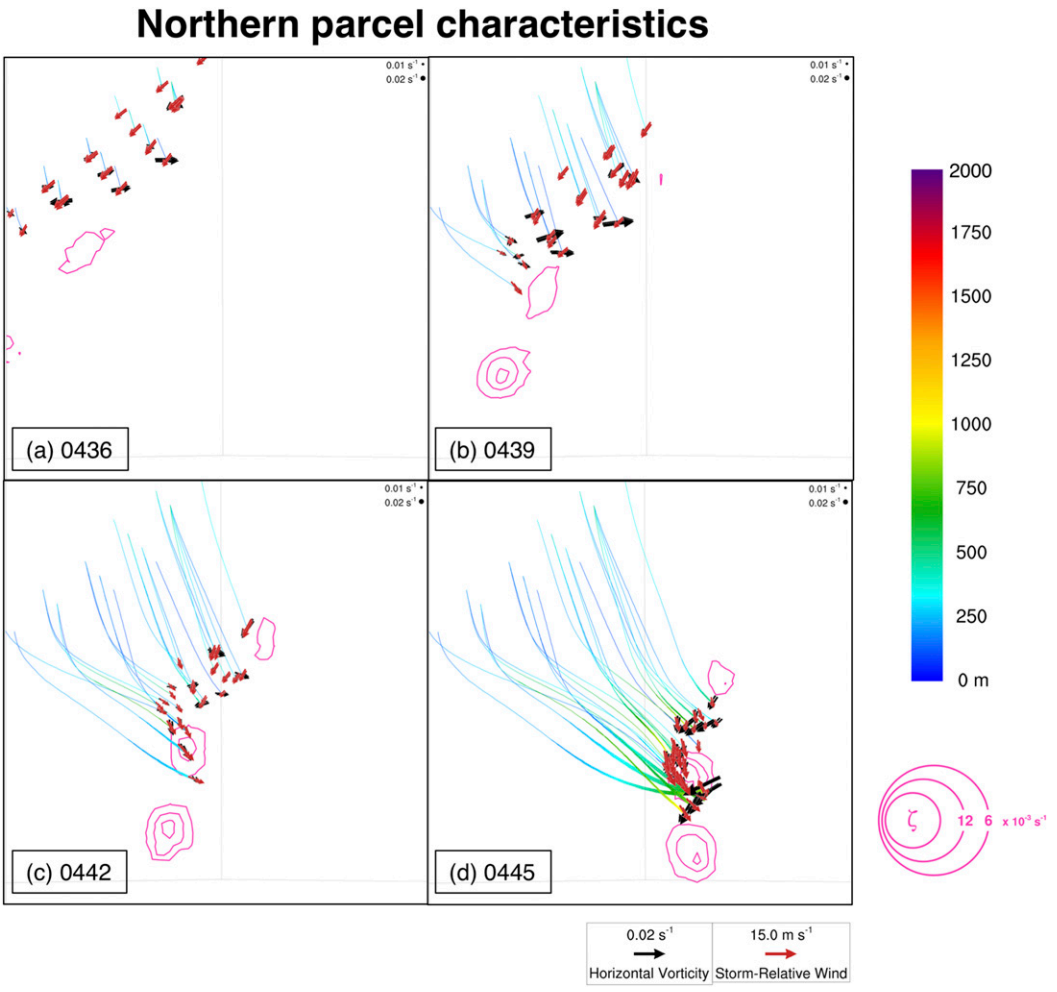

FIG. 18. As in Fig. 17, but for the parcels from the northern airstream.

the horizontal vorticity vectors of these inflowing parcels turn somewhat toward the southwest, especially for the parcels with largest vertical vorticity values closest to the mesovortex (Fig. 17d). This change in orientation of the horizontal vorticity vectors to the southwest is likely related to the baroclinic generation of horizontal vorticity along the gust front, which generates a component of horizontal vorticity generally pointing southward (for the eastward-pointing density potential temperature gradient along the north–south-oriented gust front). However, the orientation of the vorticity vectors is not altered enough to eliminate the substantial crosswise vorticity inherent in the strong low-level shear prior to the parcels reaching the developing mesovortex.

Finally, for the environmental parcels, it is notable that the strong surge of horizontal winds within the localized downdraft/rear-inflow jet that impinges on the strong southerly low-level flow enhances the convergence and forced updraft along the gust front (Fig. 14), which contributes to more rapid tilting of the horizontal vorticity than would otherwise occur without the surge. This suggests that a role of the rear-inflow surge in this case is to force the environmental inflow upward more rapidly on the equatorward side of the surge, with the geometry of the bowing gust front such that the parcels emerge near the developing mesovortex on the poleward side of the bowing gust front with significant cyclonic vertical vorticity. Furthermore, the trajectories have a small angle relative to the system-wide gust front, ensuring that the parcels will reside in the region of forced upward acceleration longer than they would otherwise be with a more westerly trajectory to the inflow parcels that is typically seen in past mesovortex simulations (e.g., Trapp and Weisman 2003; Atkins and St. Laurent 2009b). In this configuration of inflowing parcels and the gust front, without the surge and the protruding bow in the gust front (say for parcels farther south), the vorticity vectors are still tilted upward along the gust front updraft, but this

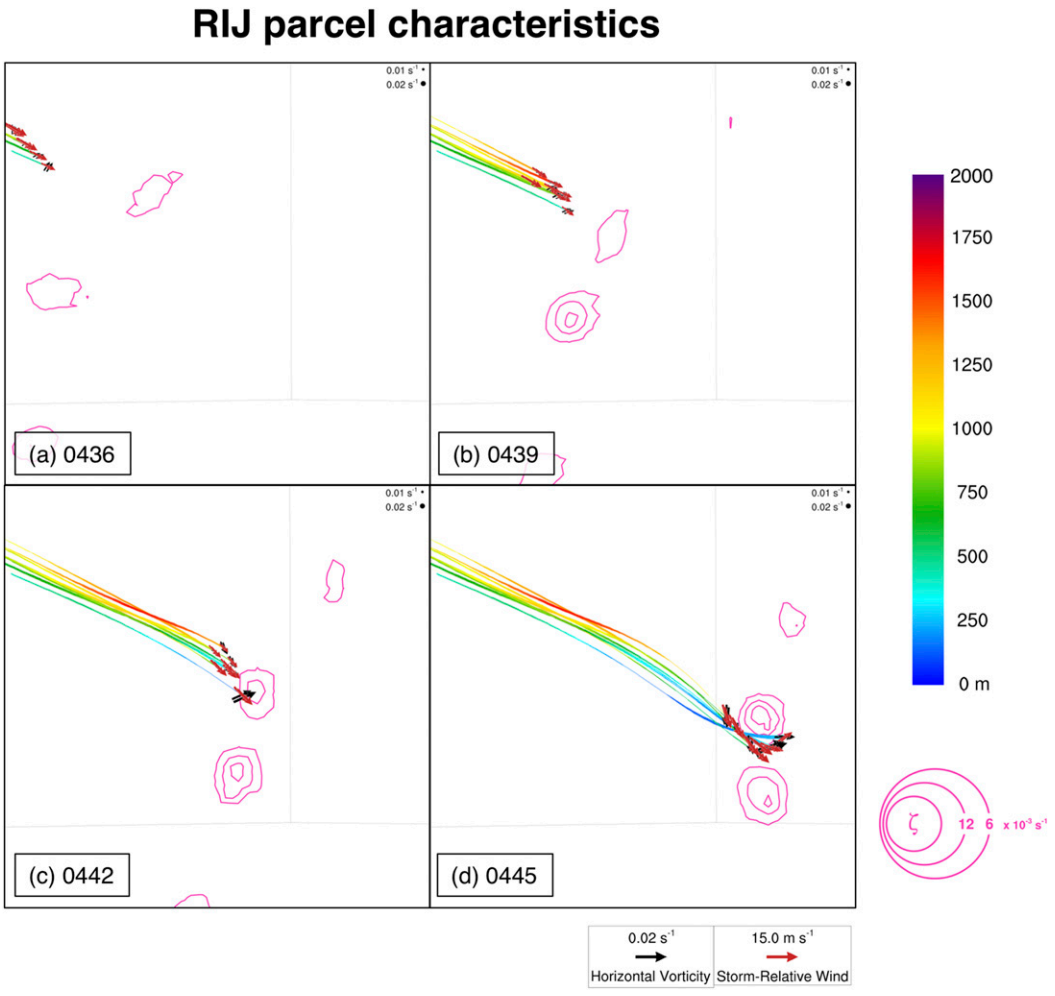

FIG. 19. As in Fig. 17, but for the parcels from the RIJ airstream.

upward tilting does not occur as quickly, and the parcels are well behind the gust front in or near the top of the cold pool by the time they acquire cyclonic vertical vorticity in this way.

The same analysis was performed for parcels originating in the northern source region (Fig. 22), with one caveat. Since the vertical vorticity derived from the integrated budget terms was close to the interpolated vertical vorticity for only a small number of parcels, those budget terms were not included in this analysis. Rather, a more qualitative analysis is performed for these parcels with updraft and mean height AGL (Fig. 22). Time series are rather short for parcels located in the mesovortex at 0441, 0443, and 0445 UTC (Figs. 22a–c). However, there is a tendency for horizontal vorticity to be more streamwise than crosswise as parcels initially rise. This same characteristic is present for parcels located within the mesovortex at 0447 UTC (Fig. 22d). From about 6 to 8 min prior to encountering the low-level mesovortex updraft, parcels rise very little and are characterized by both streamwise and crosswise horizontal vorticity. However, from about 2 to 6 min prior to encountering the low-level mesovortex updraft, horizontal vorticity increases and becomes much more streamwise. This is evident in Fig. 18, as initially chaotic, small horizontal vorticity (Figs. 18a,b) becomes oriented toward the south (Fig. 18c) and southwest (Fig. 18d) in the direction of the storm-relative wind as the parcels near the low-level updraft. This illustrates that these parcels are providing a source of primarily streamwise vorticity from low levels directly into the developing mesovortex. The streamwise vorticity develops as the parcels pass though the baroclinic zone associated with a downdraft to the west seen in the upper part of Fig. 11, most prominently from 0443 to 0451 UTC. This is similar to the import of streamwise vorticity equatorward into supercell mesocyclones shown by Orf et al. (2017) and Coffer and Parker (2017).

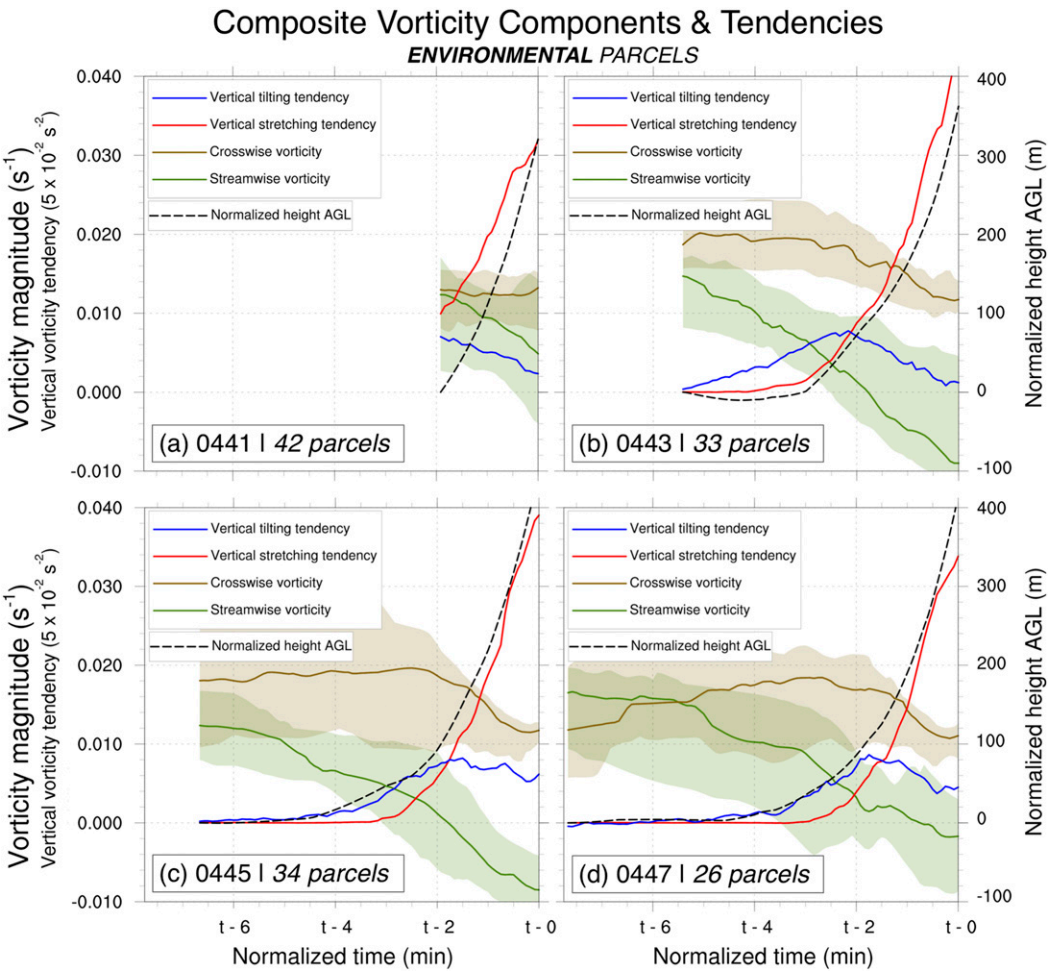

FIG. 20. Median, 10th and 90th percentiles of streamwise (green) and crosswise (brown) horizontal vorticity and mean vertical vorticity tendencies (blue: tilting; red: stretching) for parcels from the environmental source region that are located in the mesovortices at (a) 0441, (b) 0443, (c) 0445, and (d) 0447 UTC. The parcel time series are shifted in time such that the time of maximum stretching tendency (i.e., as they encounter the low-level updraft) along each trajectory occurs at the same time (defined as $t - 0$ in the figure). The heights of the parcels are normalized by their starting height (100–300 m AGL) prior to computing the mean parcel height shown by the black dashed line. This method helped to preserve signals that were susceptible to being lost by averaging over real time rather than a shifted time. The numbers of parcels in each set is given in the lower left of each panel.

Finally, the same analysis as above is shown for parcels originating in the RIJ source region (Fig. 23). Very few parcels located in the mesovortex at 0441 and 0443 UTC came from the RIJ, but for the sake of completeness, analyses for these groups of parcels are shown (Figs. 23a,b). Parcels originating in the RIJ that were located in the mesovortex at 0445 and 0447 UTC show a complex evolution (Figs. 23c,d). Both sets of parcels originated much higher than parcels from the other two source regions (~1000 vs 100–300 m AGL) and were characterized by lower values of horizontal vorticity (relative to the other source regions) that had similar magnitudes of streamwise and crosswise components. Then, 6–7 min prior to encountering the low-level updraft of the developing mesovortex, these parcels descended rapidly to 400–600 m AGL while attaining higher horizontal vorticity values. This descent is a reflection of a strong meso-γ-scale downdraft that occurred within the rear-inflow jet (depicted in the forecasts in Fig. 10 and in observations in Fig. 15). Parcels at all times generally acquired more streamwise than crosswise horizontal vorticity as they descended (especially the parcels located in the mesovortex at 0447 UTC; Fig. 23d) prior to encountering the low-level mesovortex updraft. This is seen by the initially small horizontal vorticity (Figs. 19a,b) becoming larger and oriented in the direction of the storm-relative wind (westerly) as the parcels descended and approached the low-level mesovortex (Figs. 19c,d).

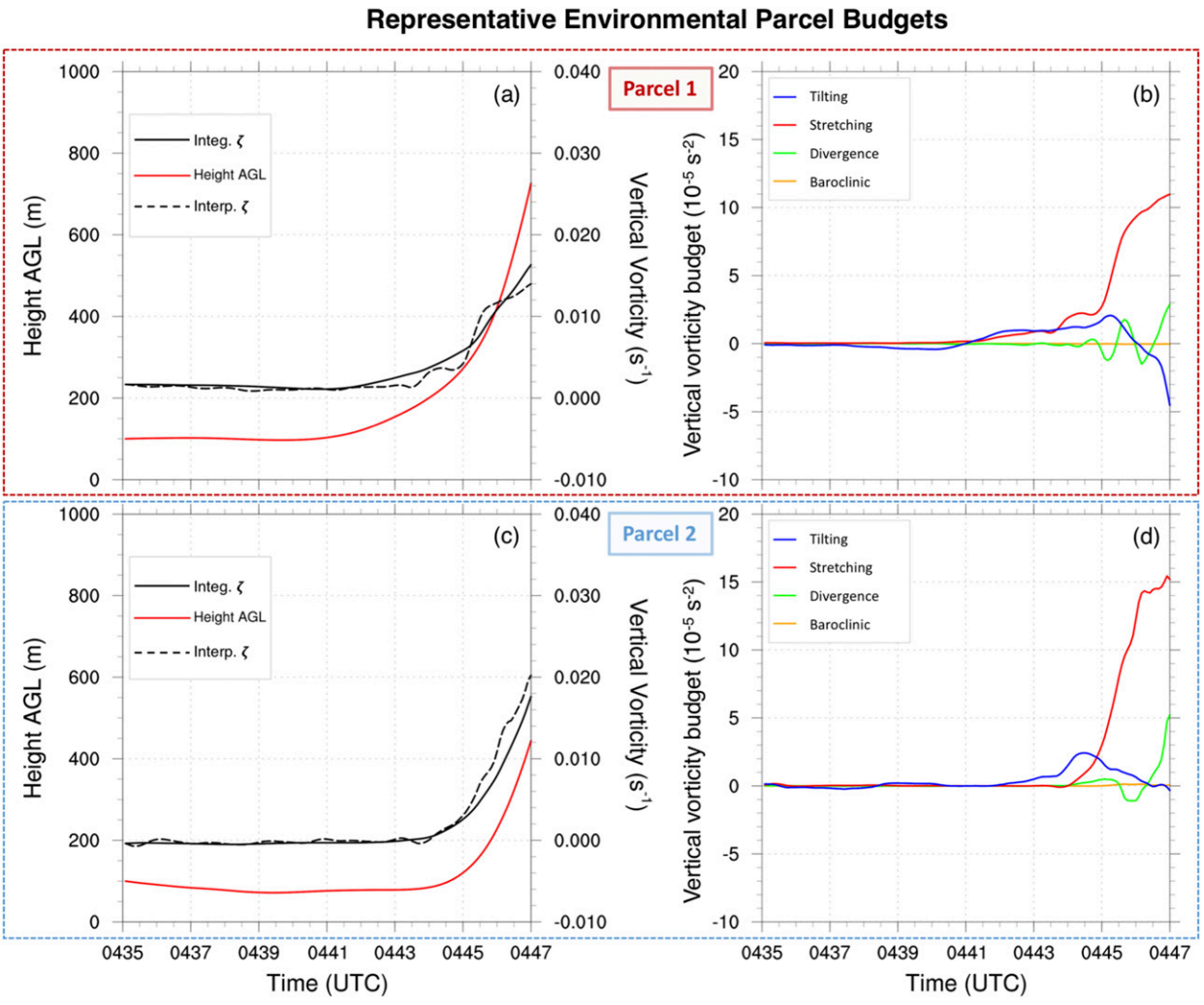

FIG. 21. Parcel quantities for two representative environmental trajectories terminating in the mesovortices at 0447 UTC. (a),(c) Integrated and interpolated vertical vorticity as well as parcel height AGL, and (b),(d) the tilting, stretching, divergence, and baroclinic vertical vorticity tendency terms. The divergence term is nonzero (especially within the low-level updraft) because incompressibility is not assumed along the trajectories.

Also, although the RIJ parcels originated nearly 1 km AGL, on average, they entered the mesovortex while rising around 600 m AGL (Fig. 23). Although inaccuracies of the vertical vorticity tendency budgets along these trajectories prevent a precise quantitative interpretation of how this streamwise vorticity is attained along the trajectories, the parcels reside in a strong horizontal gradient in density potential temperature associated with the strong rear-inflow surge/potentially cold downdraft (seen near the ground from 0445 to 0451 UTC in Fig. 11), which generates horizontal vorticity baroclinically pointed to the east-southeast along the storm-relative flow. During descent, tilting of these parcels would result in the generation of vertical vorticity (see increasing parcel trace thicknesses in Fig. 19d) via processes similar to those described by Davies-Jones and Brooks (1993) for supercell downdrafts.

In all, multiple processes influenced the development of vertical vorticity in the low-level mesovortex. Air parcels entering the mesovortex originated in both the environment ahead of the QLCS and storm-cooled air behind the main gust front. Vorticity along these trajectories evolved differently depending on the source region of the parcels, as is further discussed and summarized below.

5. Summary and discussion

This study examined processes leading to the formation of a tornadic mesovortex that occurred in southeastern South Dakota on 6 July 2015 during the PECAN

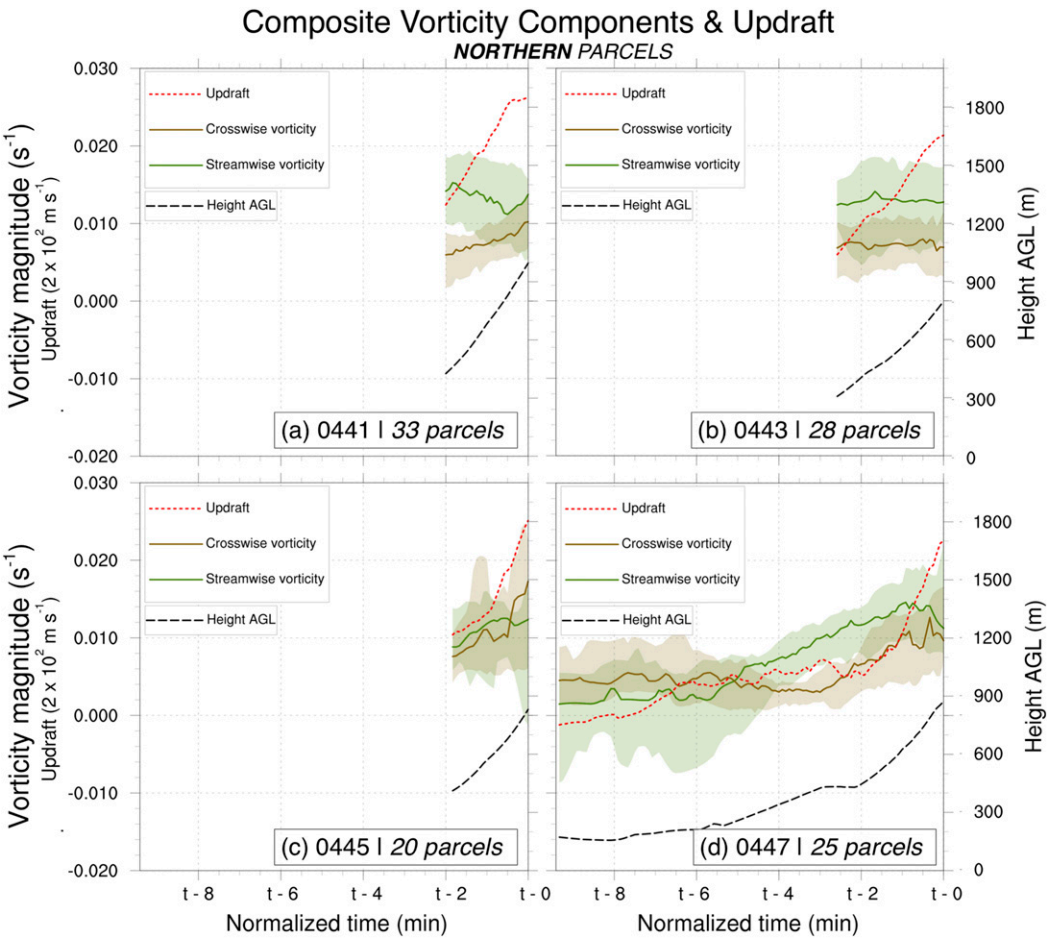

FIG. 22. As in Fig. 20, but for the parcels from the northern source region. The vertical vorticity tendency terms are not included because the integrated vertical vorticity along the parcels was close to the interpolated vertical vorticity for only a few parcels in this airstream. The times are normalized in this case according to when the parcels reach their maximum vertical velocity in the lowest 2000 m, now shown by the red dashed line.

field experiment. This mesovortex and associated MCS was well observed by multiple mobile Doppler radars, mesonets, aircraft, and profiling systems. Mobile radar, radiosonde, and aircraft data were assimilated into an ensemble system to produce analyses and forecasts of the event. The ensemble member that best captured important details in the observed event, member 30, was selected for further analysis. Most of these analyses were performed on a grid with 333-m horizontal resolution, which was sufficient to capture the meso-γ-scale details of the mesovortex and processes influencing its development.

Forecasts captured several observed mesoscale features, including the eastward-moving gust front of the main MCS, a southward-moving gust front associated with a line of broken storms to the north, and several ordinary cells that formed in the inflow region of the main MCS. Outflow from these cells ahead of the main MCS locally enhanced the synoptic-scale southerly flow, which increased low-level speed and directional shear (as similarly observed by a lidar) and created an environment more conducive for the formation of mesovortices. Also as observed, the simulated mesovortex formed along the gust front of the main MCS near the secondary gust front and to the northwest of ordinary cells. Finally, the merger of two initial mesovortices into the main mesovortex in the simulation may have also occurred in reality, as observed by KFSD.

Parcels entering the low-level mesovortex mainly originated from three different source regions: (i) the environment, (ii) the north of the mesovortex in storm-cooled air, and (iii) the northwest of the mesovortex in the vicinity of a localized downdraft/RIJ. Characteristics of parcels flowing toward the mesovortex from these different regions are summarized in Fig. 24. Parcels originating in the environment generally remained close to the surface (i.e., 100–300 m AGL), were forced

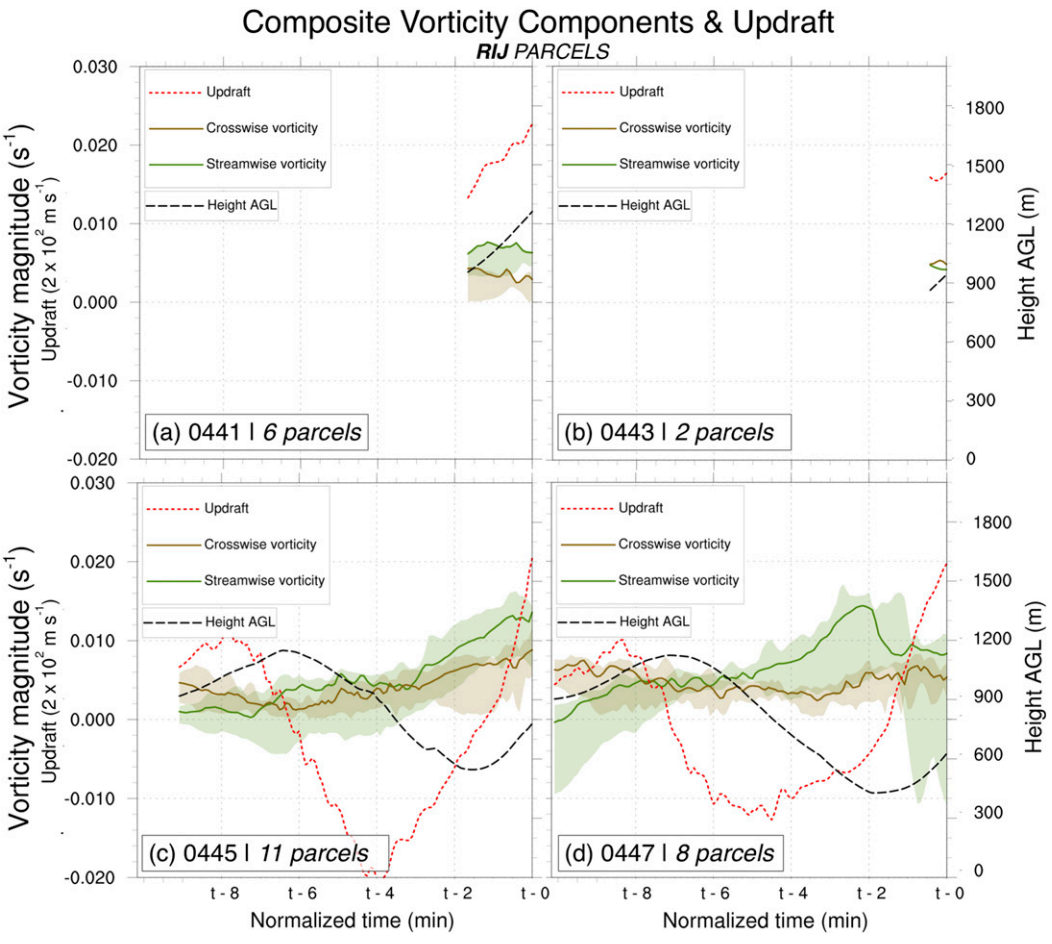

FIG. 23. As in Fig. 22, but for the parcels from the RIJ source region.

upward along the southern portion of a westerly gust front surge, and then entered the low-level mesovortex near 1 km AGL. Horizontal vorticity in the environment was predominantly crosswise close to the surface and became even more crosswise as the parcels approached the mesovortex. This horizontal vorticity was generally oriented toward the west as environmental parcels were forced up the gust front before entering the eastern edge of the mesovortex. The conversion of mostly crosswise horizontal vorticity into vertical vorticity also likely explains the presence of the simulated anticyclone to the west of the mesovortex, with line-perpendicular vortex lines (not shown) tilted upward in the mesovortex and downward in the cold pool. Parcels originating poleward of the mesovortex also began close to the surface and gradually ascended as they flowed southward. Horizontal vorticity associated with these parcels became more streamwise during their final approach to the mesovortex, at which point they were tilted upward in a streamwise manner and entered the mesovortex near 1 km AGL. Finally, RIJ parcels originated near 1 km AGL with initially small horizontal vorticity that increased during descent and became much more streamwise just prior to the parcels reaching the mesovortex. Parcels in the RIJ entered the mesovortex at lower altitudes (around 600 m AGL) than those from the other source regions and also contained the most streamwise vorticity prior to entering the low-level updraft. This streamwise horizontal vorticity was then likely converted into vertical vorticity within the low-level updraft via tilting, producing a low-level, helical mesovortex.

In all, the mesovortex genesis process outlined in this study has characteristics that are similar to the genesis of low-level mesocyclones in supercells, similar to the cyclonic-only mesovortices examined in the case study of Atkins and St. Laurent (2009b). They identified an RIJ source region of descending parcels (see Fig. 1 herein and their Fig. 9), as well as parcels originating in the environment that import horizontal vorticity inherent in the low-level shear. In both studies, parcels entering the low-level mesovortex from the environment attained cyclonic vertical vorticity via tilting of

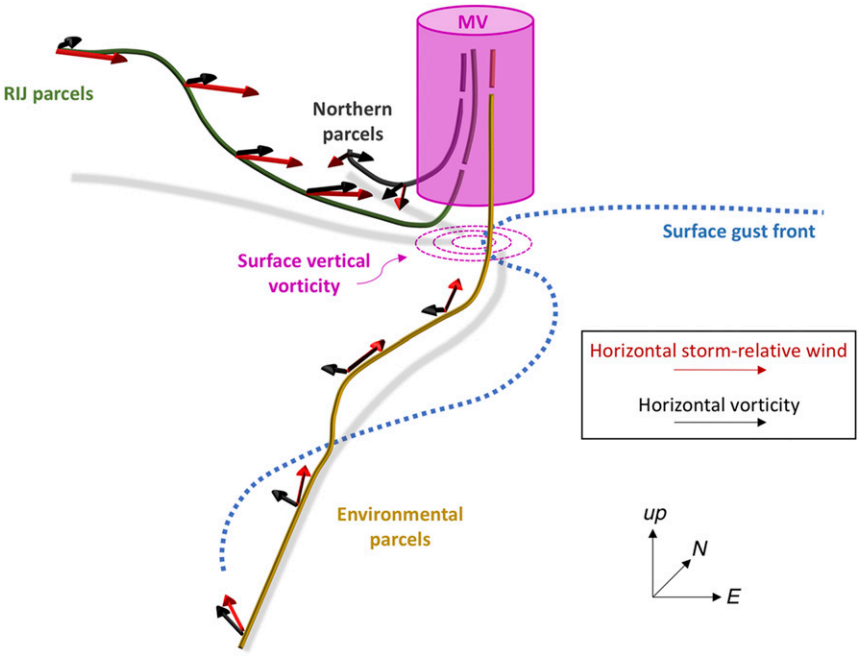

FIG. 24. Summary of the evolution of horizontal vorticity from the three airstreams identified in the development of the MV. Breaks in parcel trajectories indicate the height at which the parcel entered the mesovortices.

horizontal vorticity and subsequent stretching of vertical vorticity. However, an important difference between the processes outlined by Atkins and St. Laurent (2009b) and those here relates to how that cyclonic vertical vorticity develops from the environmental parcels. Since this process has not been identified in past literature to the extent of our knowledge, a schematic summarizing the evolution of vorticity along environmental parcels is presented in Fig. 25. In Atkins and St. Laurent (2009b), the low-level mesovortex inflow parcels come from the east and ingest largely streamwise horizontal vorticity into the updraft directly from the environment (see Fig. 1). In our analysis, the horizontal vorticity is oriented at a much larger angle to the storm-relative wind, with the horizontal vorticity vectors pointing to the west in the strong southerly flow. This results in parcels from the environment attaining cyclonic vertical vorticity through upward tilting of *crosswise* horizontal vorticity as they are forced upward along the gust front rather than through large streamwise horizontal vorticity from the environment as in Atkins and St. Laurent (2009b). The enhancement in upward forcing along this portion of the gust front provided by the enhanced convergence between the strong rear-inflow surge impinging on the inflow contributes to the strong upward tilting of the crosswise vorticity prior to the parcels entering the mesovortex. Given the largely south–north trajectory of the inflowing parcels, the parcels reside in the forced updraft along the gust front long enough to generate significant cyclonic vertical vorticity before entering the mesovortex updraft.

Parcels originating to the northwest in the RIJ originated much higher than the parcels in the other two source regions—nearly 1 km AGL—but ended up closer to the surface as they entered the developing mesovortex. These RIJ parcels contained the most streamwise vorticity and would therefore more readily produce a low-level, upright, helical mesovortex via tilting of horizontal vorticity. This process of attaining streamwise vorticity during descent is consistent with the baroclinic generation of streamwise vorticity along downdraft parcels destined for supercell mesocyclones (e.g., Davies-Jones and Brooks 1993), as similarly found by Atkins et al. (2005) and Atkins and St. Laurent (2009b).

From a forecasting standpoint, forecasters have been encouraged to examine the component of low-level vertical wind shear normal to the convective line, with magnitudes greater than $15\,m\,s^{-1}$ over the lowest 3 km AGL associated with greater potential for mesovortices along a QLCS gust front (Schaumann and Przybylinski 2012). This result stems from numerous observational analyses of mesovortex-producing QLCSs (Schaumann and Przybylinski 2012), as well as understanding gathered from numerical modeling results showing how mesovortex development occurs within environments initialized with vertical wind shear limited to the direction

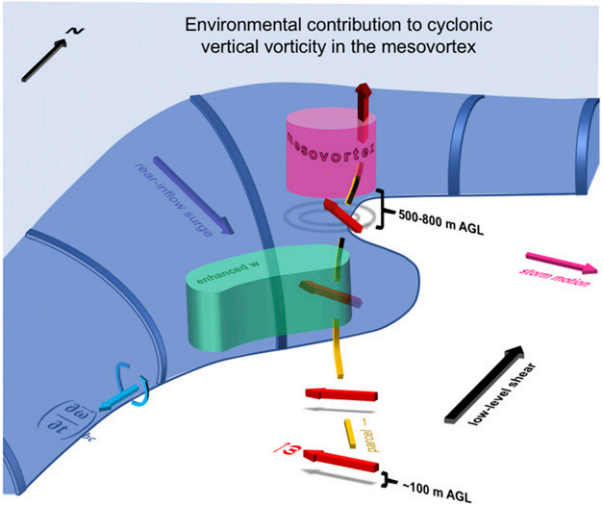

FIG. 25. Summary of the conversion of the strong low-level shear from crosswise environmental horizontal vorticity into cyclonic vertical vorticity along the rear-inflow surge (purple arrow inside the cold pool) that contributes to the strengthening MV (depicted by the pink column). The red arrows depict the full 3D vorticity vector ($\boldsymbol{\omega}$), and the blue arrow depicts the baroclinic generation of horizontal vorticity along the gust front $(\partial\boldsymbol{\omega}/\partial t)_{bc}$ that helps to turn the full vorticity vector toward the south while being tilted by the forced updraft along the gust front. An inflow parcel trajectory from a starting height of 100 m AGL is depicted by the broken yellow line. The enhancement in vertical velocity from the rear-inflow surge converging with the inflow parcels is shown by the green area. The black line depicts the strong sub-500-m AGL shear in the environment, and the pink arrow depicts the storm (MV) motion. Not depicted is the anticyclonic vertical vorticity on the west side of the enhanced vertical motion (green) that results from the tilting of the crosswise horizontal vorticity (see the dashed pink contours in Fig. 14).

normal to the convective line (e.g., Trapp and Weisman 2003). The stronger forced updraft along substantial cold pools that results from moderate to strong line-normal vertical wind shear (Rotunno et al. 1988) is thought to promote enhanced stretching and parcels that are not swept quickly over the gust front in the more erect updrafts in these environments. However, in the present study, the low-level vertical wind shear is complex and undergoes significant evolution as the MCS approaches. A layer of line-normal shear (relative to the main MCS cold pool) of 10–15 m s^{-1} exists from ~0.3 to 1.2 km AGL prior to modification (see Figs. 4 and 13a–d), but this line-normal wind shear becomes smaller with time as the system approaches (Figs. 13e,f). This is especially true in the lowest ~500 m AGL with increasing southerly winds with height in both observed and simulated hodographs (Figs. 13e,f). This very large vertical wind shear in the lowest ~500 m AGL is oriented at a small angle to the gust front, and it is the horizontal vorticity associated with this line-parallel vertical wind shear below 500 m AGL that is shown to contribute to the cyclonic vertical vorticity of the mesovortex from environmental parcels. Therefore, it is shown that this configuration of wind shear can still contribute to mesovortices stemming from the low-level shear through the tilting of crosswise horizontal vorticity in the south-southeasterly storm-relative flow, as the parcels reside in the zone of forced ascent for longer periods than they otherwise would with a more westerly trajectory seen in past studies of mesovortex environmental inflow. Furthermore, the strong rear-inflow surge acts to temporarily enhance the convergence and forced uplift of these parcels despite the suboptimal shear configuration and relatively small line-normal vertical wind shear magnitude [in the sense of Rotunno et al. (1988)]. Because of the bowing section of the gust front, the parcels emerge on the poleward side of the bowing segment with cyclonic vertical vorticity near the developing mesovortex. Without the bowing segment, parcels emerge well behind the gust front away from the convective updrafts along the leading edge of the cold pool. Indeed, a local surge in rear inflow along the QLCS gust front is one of the ingredients associated with strong and potentially tornadic mesovortices by Schaumann and Przybylinski (2012). This serves as evidence that QLCS mesovortices can still occur and be tornadic even with a low-level shear vector that is largely parallel to the gust front and relatively small line-normal wind shear.

From a numerical weather prediction standpoint, current limitations of mesovortex predictability are clear. Rapid strengthening and decay occurred in under 20 min, similar to observations of the event and well within what is typical for tornadic mesovortices (Trapp et al. 2005). Thus, forecasting mesovortices at least requires high-resolution spatial grids with frequent output times (e.g., every 5 min or less) that are currently unavailable in real-time operational settings. If such a tool was available, forecasters would then need to compare model output with real-time observations, including gust front locations and environmental boundaries. In all, the ensemble forecasting system used here, which has since evolved into the NEWS-e (Wheatley et al. 2015; Jones et al. 2016), showed skill in forecasting even storm-scale aspects of this mesovortex event and would be beneficial to operational forecasters once computational capabilities allow for it.

Acknowledgments. This study was supported by National Science Foundation Grant 1359726 and by a National Science Foundation Graduate Student Fellowship obtained by the first author. The authors thank Conrad Ziegler for helpful discussion of topics related to this case. We also thank all participants of PECAN for

becoming temporarily nocturnal and for their dedication in collecting the data used in this study. A NOAA/Office of Atmospheric Research (OAR)/Office of Weather and Air Quality (OWAQ) award provided all mobile sounding expendables used by the CSU and two NSSL sounding vehicles during PECAN. Simulations were performed on the Cray supercomputer at NSSL obtained as part of the NOAA Warn-on-Forecast program. We thank Gerry Creager and Kent Knopfmeier for their support in using the ensemble analysis and forecast system on this machine. Several figures were created using the NCAR Command Language version 6.2.1 (https://doi.org/10.5065/D6WD3XH5).

REFERENCES

Aksoy, A., D. C. Dowell, and C. Snyder, 2009: A multicase comparative assessment of the ensemble Kalman filter for assimilation of radar observations. Part I: Storm-scale analyses. *Mon. Wea. Rev.*, **137**, 1805–1824, https://doi.org/10.1175/2008MWR2691.1.

——, ——, and ——, 2010: A multicase comparative assessment of the ensemble Kalman filter for assimilation of radar observations. Part II: Short-range ensemble forecasts. *Mon. Wea. Rev.*, **138**, 1273–1292, https://doi.org/10.1175/2009MWR3086.1.

Anderson, J. L., T. Hoar, K. Raeder, H. Liu, N. Collins, R. Torn, and A. Arellano, 2009: The Data Assimilation Research Testbed: A community facility. *Bull. Amer. Meteor. Soc.*, **90**, 1283–1296, https://doi.org/10.1175/2009BAMS2618.1.

Ashley, W. S., 2007: Spatial and temporal analysis of tornado fatalities in the United States: 1880–2005. *Wea. Forecasting*, **22**, 1214–1228, https://doi.org/10.1175/2007WAF2007004.1.

——, A. J. Krmenec, and R. Schwantes, 2008: Vulnerability due to nocturnal tornadoes. *Wea. Forecasting*, **23**, 795–807, https://doi.org/10.1175/2008WAF2222132.1.

Atkins, N. T., and M. St. Laurent, 2009a: Bow echo mesovortices. Part I: Processes that influence their damaging potential. *Mon. Wea. Rev.*, **137**, 1497–1513, https://doi.org/10.1175/2008MWR2649.1.

——, and ——, 2009b: Bow echo mesovortices. Part II: Their genesis. *Mon. Wea. Rev.*, **137**, 1514–1532, https://doi.org/10.1175/2008MWR2650.1.

——, J. M. Arnott, R. W. Przybylinski, R. A. Wolf, and B. D. Ketcham, 2004: Vortex structure and evolution within bow echoes. Part I: Single-Doppler and damage analysis of the 29 June 1998 derecho. *Mon. Wea. Rev.*, **132**, 2224–2242, https://doi.org/10.1175/1520-0493(2004)132<2224:VSAEWB>2.0.CO;2.

——, C. S. Bouchard, R. W. Przybylinski, R. J. Trapp, and G. Schmocker, 2005: Damaging surface wind mechanisms within the 10 June 2003 Saint Louis bow echo during BAMEX. *Mon. Wea. Rev.*, **133**, 2275–2296, https://doi.org/10.1175/MWR2973.1.

Barnes, S. L., 1964: A technique for maximizing details in numerical weather map analysis. *J. Appl. Meteor.*, **3**, 396–409, https://doi.org/10.1175/1520-0450(1964)003<0396:ATFMDI>2.0.CO;2.

Bernardet, L. R., and W. R. Cotton, 1998: Multiscale evolution of a derecho-producing mesoscale convective system. *Mon. Wea. Rev.*, **126**, 2991–3015, https://doi.org/10.1175/1520-0493(1998)126<2991:MEOADP>2.0.CO;2.

Bodine, D. J., and K. L. Rasmussen, 2017: Evolution of mesoscale convective system organizational structure and convective line propagation. *Mon. Wea. Rev.*, **145**, 3419–3440, https://doi.org/10.1175/MWR-D-16-0406.1.

Coffer, B. E., and M. D. Parker, 2017: Simulated supercells in nontornadic and tornadic VORTEX2 environments. *Mon. Wea. Rev.*, **145**, 149–180, https://doi.org/10.1175/MWR-D-16-0226.1.

Coniglio, M. C., S. M. Hitchcock, and K. H. Knopfmeier, 2016: Impact of assimilating preconvective upsonde observations on short-term forecasts of convection observed during MPEX. *Mon. Wea. Rev.*, **144**, 4301–4325, https://doi.org/10.1175/MWR-D-16-0091.1.

Cotton, W. R., M. S. Lin, R. L. McAnelly, and C. J. Tremback, 1989: A composite model of mesoscale convective complexes. *Mon. Wea. Rev.*, **117**, 765–783, https://doi.org/10.1175/1520-0493(1989)117<0765:ACMOMC>2.0.CO;2.

Davies-Jones, R., and H. Brooks, 1993: Mesocyclogenesis from a theoretical perspective. *The Tornado: Its Structure, Dynamics, Prediction, and Hazards*, *Geophys. Monogr.*, Vol. 79, Amer. Geophys. Union, 105–114, https://doi.org/10.1029/GM079p0105.

Dowell, D. C., L. J. Wicker, and D. J. Stensrud, 2004: High-resolution analyses of the 8 May 2003 Oklahoma City storm. Part II: EnKF data assimilation and forecast experiments. *22nd Conf. on Severe Local Storms*, Hyannis, MA, Amer. Meteor. Soc., 12.5, https://ams.confex.com/ams/11aram22sls/techprogram/paper_81393.htm.

——, ——, and C. Snyder, 2011: Ensemble Kalman filter assimilation of radar observations of the 8 May 2003 Oklahoma City supercell: Influences of reflectivity observations on storm-scale analyses. *Mon. Wea. Rev.*, **139**, 272–294, https://doi.org/10.1175/2010MWR3438.1.

Evensen, G., 1994: Sequential data assimilation with a nonlinear quasi-geostrophic model using Monte Carlo methods to forecast error statistics. *J. Geophys. Res.*, **99**, 10 143–10 162, https://doi.org/10.1029/94JC00572.

Forbes, G. S., and R. M. Wakimoto, 1983: A concentrated outbreak of tornadoes, downbursts and microbursts, and implications regarding vortex classification. *Mon. Wea. Rev.*, **111**, 220–236, https://doi.org/10.1175/1520-0493(1983)111<0220:ACOOTD>2.0.CO;2.

Funk, T. W., K. E. Darmofal, J. D. Kirkpatrick, V. L. DeWald, R. W. Przybylinski, G. K. Schmocker, and Y. J. Lin, 1999: Storm reflectivity and mesocyclone evolution associated with the 15 April 1994 squall line over Kentucky and southern Indiana. *Wea. Forecasting*, **14**, 976–993, https://doi.org/10.1175/1520-0434(1999)014<0976:SRAMEA>2.0.CO;2.

Geerts, B., and Coauthors, 2017: The 2015 Plains Elevated Convection At Night field project. *Bull. Amer. Meteor. Soc.*, **98**, 767–786, https://doi.org/10.1175/BAMS-D-15-00257.1.

Helmus, J., and S. Collis, 2016: The Python ARM Radar Toolkit (Py-ART), a library for working with weather radar data in the Python programming language. *J. Open Res. Software*, **4**, e25, https://doi.org/10.5334/jors.119.

Hitchcock, S. M., M. C. Coniglio, and K. H. Knopfmeier, 2016: Impact of MPEX upsonde observations on ensemble analyses and forecasts of the 31 May 2013 convective event over Oklahoma. *Mon. Wea. Rev.*, **144**, 2889–2913, https://doi.org/10.1175/MWR-D-15-0344.1.

Jones, T. A., K. Knopfmeier, D. Wheatley, G. Creager, P. Minnis, and R. Palikonda, 2016: Storm-scale data assimilation and ensemble forecasting with the NSSL Experimental Warn-on-Forecast System. Part II: Combined radar and satellite data experiments. *Wea. Forecasting*, **31**, 297–327, https://doi.org/10.1175/WAF-D-15-0107.1.

Lawson, J. R., J. S. Kain, N. Yussouf, D. C. Dowell, D. M. Wheatley, K. H. Knopfmeier, and T. A. Jones, 2018: Advancing from

convection-allowing NWP to Warn-on-Forecast: Evidence of progress. *Wea. Forecasting*, **33**, 599–607, https://doi.org/10.1175/WAF-D-17-0145.1.

Lee, B. D., and R. B. Wilhelmson, 1997a: The numerical simulation of non-supercell tornadogenesis. Part I: Initiation and evolution of pretornadic misocyclone circulations along a dry outflow boundary. *J. Atmos. Sci.*, **54**, 32–60, https://doi.org/10.1175/1520-0469(1997)054<0032:TNSONS>2.0.CO;2.

——, and ——, 1997b: The numerical simulation of non-supercell tornadogenesis. Part II: Evolution of a family of tornadoes along a weak outflow boundary. *J. Atmos. Sci.*, **54**, 2387–2415, https://doi.org/10.1175/1520-0469(1997)054<2387:TNSONT>2.0.CO;2.

Mahale, V. N., J. A. Brotzge, and H. B. Bluestein, 2012: An analysis of vortices embedded within a quasi-linear convective system using X-band polarimetric radar. *Wea. Forecasting*, **27**, 1520–1537, https://doi.org/10.1175/WAF-D-11-00135.1.

Markowski, P. M., 2016: An idealized numerical simulation investigation of the effects of surface drag on the development of near-surface vertical vorticity in supercell thunderstorms. *J. Atmos. Sci.*, **73**, 4349–4385, https://doi.org/10.1175/JAS-D-16-0150.1.

——, and Y. P. Richardson, 2009: Tornadogenesis: Our current understanding, forecasting considerations, and questions to guide future research. *Atmos. Res.*, **93**, 3–10, https://doi.org/10.1016/j.atmosres.2008.09.015.

——, and G. H. Bryan, 2016: LES of laminar flow in the PBL: A potential problem for convective storm simulations. *Mon. Wea. Rev.*, **144**, 1841–1850, https://doi.org/10.1175/MWR-D-15-0439.1.

Mashiko, W., 2016b: A numerical study of the 6 May 2012 Tsukuba City supercell tornado. Part II: Mechanisms of tornadogenesis. *Mon. Wea. Rev.*, **144**, 3077–3098, https://doi.org/10.1175/MWR-D-15-0122.1.

Menard, R. D., and J. M. Fritsch, 1989: A mesoscale convective complex-generated inertially stable warm core vortex. *Mon. Wea. Rev.*, **117**, 1237–1261, https://doi.org/10.1175/1520-0493(1989)117<1237:AMCCGI>2.0.CO;2.

Miles, J. W., and L. N. Howard, 1964: Note on a heterogeneous shear flow. *J. Fluid Mech.*, **20**, 331–336, https://doi.org/10.1017/S0022112064001252.

Miller, P. A., M. Barth, L. Benjamin, R. Artz, and W. Pendergrass, 2007: MADIS support for UrbaNet. *14th Symp. on Meteorological Observations and Instrumentation*, San Antonio, TX, Amer. Meteor. Soc., JP2.5, https://ams.confex.com/ams/87ANNUAL/techprogram/paper_119116.htm.

Newman, J. F., and P. L. Heinselman, 2012: Evolution of a quasi-linear convective system sampled by phased array radar. *Mon. Wea. Rev.*, **140**, 3467–3486, https://doi.org/10.1175/MWR-D-12-00003.1.

Orf, L., R. Wilhelmson, B. Lee, C. Finley, and A. Houston, 2017: Evolution of a long-track violent tornado within a simulated supercell. *Bull. Amer. Meteor. Soc.*, **98**, 45–68, https://doi.org/10.1175/BAMS-D-15-00073.1.

Orlanski, I., 1975: A rational subdivision of scales for atmospheric processes. *Bull. Amer. Meteor. Soc.*, **56**, 527–534, https://doi.org/10.1175/1520-0477-56.5.527.

Parker, M. D., and J. M. Dahl, 2015: Production of near-surface vertical vorticity by idealized downdrafts. *Mon. Wea. Rev.*, **143**, 2795–2816, https://doi.org/10.1175/MWR-D-14-00310.1.

Przybylinski, R. W., 1995: The bow echo: Observations, numerical simulations, and severe weather detection methods. *Wea. Forecasting*, **10**, 203–218, https://doi.org/10.1175/1520-0434(1995)010<0203:TBEONS>2.0.CO;2.

——, G. K. Schmocker, and Y. J. Lin, 2000: A study of storm and vortex morphology during the 'intensifying stage' of severe wind mesoscale convective systems. Preprints, *20th Conf. on Severe Local Storms*, Orlando, FL, Amer. Meteor. Soc., 6.2, https://ams.confex.com/ams/Sept2000/webprogram/Paper16397.html.

Richter, H., J. Peter, and S. Collis, 2014: Analysis of a destructive wind storm on 16 November 2008 in Brisbane, Australia. *Mon. Wea. Rev.*, **142**, 3038–3060, https://doi.org/10.1175/MWR-D-13-00405.1.

Roberts, B., M. Xue, A. D. Schenkman, and D. T. Dawson, 2016: The role of surface drag in tornadogenesis within an idealized supercell simulation. *J. Atmos. Sci.*, **73**, 3371–3395, https://doi.org/10.1175/JAS-D-15-0332.1.

Rotunno, R., J. B. Klemp, and M. L. Weisman, 1988: A theory for strong, long-lived squall lines. *J. Atmos. Sci.*, **45**, 463–485, https://doi.org/10.1175/1520-0469(1988)045<0463:ATFSLL>2.0.CO;2.

Schaumann, J. S., and R. W. Przybylinski, 2012: Operational application of 0–3 km bulk shear vectors in assessing quasi linear convective system mesovortex and tornado potential. *26th Conf. on Severe Local Storms*, Nashville, TN, Amer. Meteor. Soc., 142, https://ams.confex.com/ams/26SLS/webprogram/Paper212008.html.

Schenkman, A. D., M. Xue, A. Shapiro, K. Brewster, and J. Gao, 2011a: The analysis and prediction of the 8–9 May 2007 Oklahoma tornadic mesoscale convective system by assimilating WSR-88D and CASA radar data using 3DVAR. *Mon. Wea. Rev.*, **139**, 224–246, https://doi.org/10.1175/2010MWR3336.1.

——, ——, ——, ——, and ——, 2011b: Impact of CASA radar and Oklahoma Mesonet data assimilation on the analysis and prediction of tornadic mesovortices in an MCS. *Mon. Wea. Rev.*, **139**, 3422–3445, https://doi.org/10.1175/MWR-D-10-05051.1.

——, ——, and ——, 2012: Tornadogenesis in a simulated mesovortex within a mesoscale convective system. *J. Atmos. Sci.*, **69**, 3372–3390, https://doi.org/10.1175/JAS-D-12-038.1.

——, ——, and M. Hu, 2014: Tornadogenesis in a high-resolution simulation of the 8 May 2003 Oklahoma City supercell. *J. Atmos. Sci.*, **71**, 130–154, https://doi.org/10.1175/JAS-D-13-073.1.

Seibert, P., 1993: Convergence and accuracy of numerical methods for trajectory calculations. *J. Appl. Meteor.*, **32**, 558–566, https://doi.org/10.1175/1520-0450(1993)032<0558:CAAONM>2.0.CO;2.

Skamarock, W. C., and J. B. Klemp, 2008: A time-split nonhydrostatic atmospheric model for weather research and forecasting applications. *J. Comput. Phys.*, **227**, 3465–3485, https://doi.org/10.1016/j.jcp.2007.01.037.

Snook, N., M. Xue, and Y. Jung, 2011: Analysis of a tornadic mesoscale convective vortex based on ensemble Kalman filter assimilation of CASA X-band and WSR-88D radar data. *Mon. Wea. Rev.*, **139**, 3446–3468, https://doi.org/10.1175/MWR-D-10-05053.1.

Snyder, C., and F. Zhang, 2003: Assimilation of simulated Doppler radar observations with an ensemble Kalman filter. *Mon. Wea. Rev.*, **131**, 1663–1677, https://doi.org/10.1175//2555.1.

Thompson, G., R. M. Rasmussen, and K. Manning, 2004: Explicit forecasts of winter precipitation using an improved bulk microphysics scheme. Part I: Description and sensitivity analysis. *Mon. Wea. Rev.*, **132**, 519–542, https://doi.org/10.1175/1520-0493(2004)132<0519:EFOWPU>2.0.CO;2.

Tong, M., and M. Xue, 2005: Ensemble Kalman filter assimilation of Doppler radar data with a compressible nonhydrostatic model: OSS experiments. *Mon. Wea. Rev.*, **133**, 1789–1807, https://doi.org/10.1175/MWR2898.1.

Trapp, R. J., and M. L. Weisman, 2003: Low-level mesovortices within squall lines and bow echoes. Part II: Their genesis and implications. *Mon. Wea. Rev.*, **131**, 2804–2823, https://doi.org/10.1175/1520-0493(2003)131<2804:LMWSLA>2.0.CO;2.

——, E. D. Mitchell, G. A. Tipton, D. W. Effertz, A. I. Watson, D. L. Andra Jr., and M. A. Magsig, 1999: Descending and nondescending tornadic vortex signatures detected by WSR-88Ds. *Wea. Forecasting*, **14**, 625–639, https://doi.org/10.1175/1520-0434(1999)014<0625:DANTVS>2.0.CO;2.

——, S. A. Tessendorf, E. S. Godfrey, and H. E. Brooks, 2005: Tornadoes from squall lines and bow echoes. Part I: Climatological distribution. *Wea. Forecasting*, **20**, 23–34, https://doi.org/10.1175/WAF-835.1.

Wakimoto, R. M., H. V. Murphey, A. Nester, D. P. Jorgensen, and N. T. Atkins, 2006a: High winds generated by bow echoes. Part I: Overview of the Omaha bow echo 5 July 2003 storm during BAMEX. *Mon. Wea. Rev.*, **134**, 2793–2812, https://doi.org/10.1175/MWR3215.1.

——, ——, C. A. Davis, and N. T. Atkins, 2006b: High winds generated by bow echoes. Part II: The relationship between the mesovortices and damaging straight-line winds. *Mon. Wea. Rev.*, **134**, 2813–2829, https://doi.org/10.1175/MWR3216.1.

Weisman, M. L., 1992: The role of convectively generated rear-inflow jets in the evolution of long-lived mesoconvective systems. *J. Atmos. Sci.*, **49**, 1826–1847, https://doi.org/10.1175/1520-0469(1992)049<1826:TROCGR>2.0.CO;2.

——, 1993: The genesis of severe, long-lived bow echoes. *J. Atmos. Sci.*, **50**, 645–670, https://doi.org/10.1175/1520-0469(1993)050<0645:TGOSLL>2.0.CO;2.

——, and R. J. Trapp, 2003: Low-level mesovortices within squall lines and bow echoes. Part I: Overview and dependence on environmental shear. *Mon. Wea. Rev.*, **131**, 2779–2803, https://doi.org/10.1175/1520-0493(2003)131<2779:LMWSLA>2.0.CO;2.

Wheatley, D. M., and R. J. Trapp, 2008: The effect of mesoscale heterogeneity on the genesis and structure of mesovortices within quasi-linear convective systems. *Mon. Wea. Rev.*, **136**, 4220–4241, https://doi.org/10.1175/2008MWR2294.1.

——, K. H. Knopfmeier, T. A. Jones, and G. J. Creager, 2015: Storm-scale data assimilation and ensemble forecasting with the NSSL Experimental Warn-on-Forecast System. Part I: Radar data experiments. *Wea. Forecasting*, **30**, 1795–1817, https://doi.org/10.1175/WAF-D-15-0043.1.

Xu, X., M. Xue, and Y. Wang, 2015: The genesis of mesovortices within a real-data simulation of a bow echo system. *J. Atmos. Sci.*, **72**, 1963–1986, https://doi.org/10.1175/JAS-D-14-0209.1.

Yussouf, N., and D. J. Stensrud, 2010: Impact of phased-array radar observations over a short assimilation period: Observing system simulation experiments using an ensemble Kalman filter. *Mon. Wea. Rev.*, **138**, 517–538, https://doi.org/10.1175/2009MWR2925.1.

——, J. Gao, D. J. Stensrud, and G. Ge, 2013: The impact of mesoscale environmental uncertainty on the prediction of a tornadic supercell storm using ensemble data assimilation approach. *Adv. Meteor.*, **2013**, 731647, https://doi.org/10.1155/2013/731647.

Zhang, F., C. Snyder, and J. Sun, 2004: Impacts of initial estimate and observation availability on convective-scale data assimilation with an ensemble Kalman filter. *Mon. Wea. Rev.*, **132**, 1238–1253, https://doi.org/10.1175/1520-0493(2004)132<1238:IOIEAO>2.0.CO;2.